

TRANSITION RADIATION, NON-HERMITICITY
AND TEMPORAL MODULATION IN PHOTONIC
AND LATTICE SYSTEMS

A Dissertation

Presented to the Faculty of the Graduate School

of Cornell University

in Partial Fulfillment of the Requirements for the Degree of

Doctor of Philosophy

by

Yang Yu

December 2021

© 2021 Yang Yu

ALL RIGHTS RESERVED

TRANSITION RADIATION, NON-HERMITICITY AND TEMPORAL
MODULATION IN PHOTONIC AND LATTICE SYSTEMS

Yang Yu, Ph.D.

Cornell University 2021

This dissertation is a compilation of three independent, but nonetheless connected papers.

The first one extends the concept of transition radiation into photonic crystals, that is, the radiation emitted when a charge cross the boundary of two different photonic crystals. To simplify the problem and for practical considerations, the focus is put on the edge waves emitted that travel along the boundary, if there is any supported. For frequencies where only edge waves exist, the field and thus the power spectrum are calculated conveniently using the Bloch mode expansion thanks to the remaining translational symmetry of the system. An example is then given where topological protected edge waves between two topologically distinct photonic crystal domains are excited by a moving charge. For this specific problem, the concept of quasi-phase matching is introduced which provides a very good understanding to the power spectrum.

The second paper demonstrates that eigendecomposition is not suited for the analysis of non-Hermitian systems. Instead, the Jordan decomposition should be used. While in the strict sense the Jordan decomposition is also not stable to compute numerically, if the system hosts a few number of spectrally isolated states, then it makes sense to separate this invariant subspace and complete the “partial Jordan decomposition”. A numerical recipe on how to achieve this is presented, based on the stable and well-studied Schur decomposition. An example of a non-

Hermitian quadrupole insulator is then given to show how this “partial Jordan decomposition” is helpful to our understanding of the response of the system to drives with frequencies close to the eigenfrequencies of those spectrally isolated states.

The third paper originates from the apparent discrepancy between Floquet crystals and the so-called “photonic time crystals”, both are systems periodically varying in time, but the former having bandgaps in frequency while the latter having bandgaps in wavevector. This discrepancy is resolved by realising that if photonic systems are described by first order (in time) differential equations instead of second order ones, then varying permittivity alone is actually a non-Hermitian perturbation, even though the permittivity is always real. The paper goes on to discuss some criteria of possible bandgaps opening in frequency or wavevector or both directions, in either solid state systems or photonic systems. Multiple examples are given and finally the difference between a gap in frequency and one in wavevector, as well as an interface in time and one in space is discussed.

BIOGRAPHICAL SKETCH

Yang Yu received his B.S. in Physics from Peking University (Beijing, P. R. China) in 2015 with a thesis titled “Studying Graphene Using Lattice Field Theory” under the supervision of Professor Chuan Liu (Ph.D., University of California, San Diego, 1994). He received his M.S. in Applied Physics at Cornell in 2019, where he has worked as a Graduate Research Assistant since 2016.

谨以此文献给我的父母。

ACKNOWLEDGEMENTS

During my five and a half years of stay at the School of Applied & Engineering Physics (AEP) at Cornell University, I received enormous help from many people, without which I believe it would be nearly impossible to finish my study. Thus I want to express my appreciation to them here.

First, I would like to thank my advisor, Professor Gennady Shvets, for his continued guidance and support. He encourages me not to be limited by his own expertise but rather explore the much broader field of physics and is always ready to listen to me talk about my discoveries and provide help when I run into difficulties. I was greatly impressed by his enthusiasm, and he never stops throwing out interesting ideas. In fact, the original idea of my work on transition radiation in photonic crystals should be credited to him.

I would also like to thank the other members of my committee (Professor Daniel Ralph and Professor Francesco Monticone) for taking the time to talk to me and giving me important suggestions during the program. I also want to thank the following Professors at AEP, Physics Department, and other departments from whom I benefit from their lectures or guidance: Professor Chao-Ming Jian, Professor Katja Nowack, Professor Austin Benson and Professor Gregory Fuchs.

I was lucky to have a group of graduate students, postdocs and research scientists willing to discuss with me, challenge me, and help me. Among those I learned the most from Tzuhsuan Ma, Doctor Zhiyuan Fan, Kueifu Lai, Minwoo Jung, Doctor Maxim Shcherbakov, Doctor Vladimir Khudik, Yandong Li, Doctor Simeon Trendafilov, Ran Gladstone, Robert Delgado and Tianhong Wang.

Cynthia Reynolds helped a lot as the Graduate Field Assistant of AEP.

I also want to thank my friends for their support, including but not limited to: Y. Xie, Y. Yao, Z. He, Y. Fang, C. Wan, J. Luo.

TABLE OF CONTENTS

Biographical Sketch	iii
Dedication	iv
Acknowledgements	v
Table of Contents	vi
1 Transition Edge Radiation in Photonic Crystals	1
1.1 Introduction	1
1.2 General Formalism	3
1.2.1 Formation Length	6
1.3 Excitation of topological kink states	7
1.4 Experimental Validation	11
1.5 Conclusions	13
1.6 Supplemental Material	13
1.6.1 Some other configurations using TR to excite guided modes	13
1.6.2 Asymptotic behavior of electric field	14
1.6.3 Some useful identities of Bloch eigenmodes	15
1.6.4 Derivation of the expression of energy spectral density	17
1.6.5 Emission of surface plasmon polaritons by transition radiation	18
1.6.6 Quasi-phase matching between edge modes and the current	20
1.6.7 Experimental setup	25
1.6.8 TER-based accelerators	27
2 Application of Jordan Decomposition to Non-Hermitian Lattice Models with Spectrally-Isolated Lower Dimensional States	31
2.1 Introduction	31
2.2 Non-Bloch bulk continuum	34
2.3 Zero-energy corner states	36
2.4 Conclusions	42
2.5 Supplemental Material	43
2.5.1 Spectrum of an open-boundary non-Hermitian quadrupole insulator (QI)	43
2.5.2 Analytic verification of corner states	44
2.5.3 Additional examples of excitation of corner states in the intermediate regime	46
2.5.4 Excitation of corner states in the near-Hermitian regime	46
3 Band repulsion in condensed matter and electromagnetic systems	48
3.1 Introduction and Motivation	48
3.2 Time- and Floquet-crystals: Examples and Existence Criteria	51
3.2.1 A linearized Hamiltonian and the bandgap existence criteria	52
3.2.2 The linearized Hamiltonian: examples	54
3.3 Perturbation Theory near Band Crossings	57

3.4	Time-periodic perturbations of photonic crystals	60
3.5	Time-modulated SSH model	64
3.6	Conclusions	69
	Bibliography	70

CHAPTER 1

TRANSITION EDGE RADIATION IN PHOTONIC CRYSTALS

This Chapter was published on Physical Review Letters [101].

1.1 Introduction

Generation of electromagnetic (EM) waves by moving electric charges is one of the most fundamental phenomena in physics. While a charge must be accelerated to produce EM radiation in free space, this requirement no longer exists in optically-dense media. Even in a homogeneous isotropic medium, the Cherenkov radiation (CR) [15] by a charge travelling with a constant velocity v can be produced when the phase velocity v_{ph} of EM waves is smaller than v . In an inhomogeneous medium, transition radiation (TR) [24] – usually studied in the context of a charge crossing an interface between two media with different permittivities and/or permeabilities – can also be produced by a constant-velocity motion [84, 25, 26, 27, 32, 16, 87, 1] regardless of the magnitude of v . TR has already found numerous applications in particle detectors and beam diagnostics [87, 2]. More recently, there has been considerable interest in expanding the TR concept to more complex geometries and structures, including the resonant transition radiation [71, 72, 6, 57] in multi-interfacial materials that form a one-dimensional (1D) photonic crystal. TR has also been used to excite surface plasmon polaritons (SPPs) [27, 49] and guided modes in thin films [12, 102], which are hard to be directly excited by far-field (e.g., laser) radiation.

The key limitation of all these approaches to producing TR is that fast charged particles must be sent through a solid medium, resulting in rapid energy loss by the

electrons, as well as the inevitable incoherent emission [17]. For example, a 1 MeV electron loses all of its energy after propagating through just under 3 mm of silicon. Charging of multi-layer dielectric structures bombarded by high-charge bunches also limits their longevity [91]. Therefore, one is led to consider an intriguing yet unexplored possibility of producing TR in a photonic crystal (PhC) designed to have an empty region that provides an unobstructed path for the moving charge (see Fig. 1.1). However, the physics of TR excitation in two- and three-dimensional periodic media has not been studied either theoretically or experimentally, with a few exception of 1D multilayer films [71, 6, 57]. Even in those studies, the emphasis was on the excitation of the modified Cherenkov (i.e. bulk) radiation, and the feasibility of sending electrons through solid medium was assumed. In this Letter, we extend the concept of TR to the case of a charge crossing the interface between two PhCs and emitting *guided waves* that are localized to the interface. In particular, we consider the previously unexplored concept of TR into topologically protected edge waves (TPEWs) that exist at the domain wall between two topologically-distinct photonic topological insulators (PTIs) [30, 44, 31, 50]. We demonstrate that the moving charge breaks the time-reversal symmetry of TPEWs and enables spin- and valley-polarized emission of TPEWs that are routed into spin-locked ports. In condensed matter physics it has been shown that circularly polarized light can excite spin-locked currents on the surface of topological insulators [82]. Among practical attractions of TPEWs are their one-dimensional (i.e. localized in the other two dimensions) nature, and the ability for reflection-free propagation around sharp corners [64]. Similarly to SPPs, TPEWs cannot directly couple to bulk EM waves. However, SPPs can be also excited by moving charges via the CR mechanism [17] because their dispersion curves are below the light line ($v_{\text{ph}} < c$) due to their polaritonic nature, while TPEWs

frequently cannot be because the phase velocities of the guided EM waves typically satisfy $v_{\text{ph}} > c$.

1.2 General Formalism

We start by developing a general formalism of guided waves' excitation by a TR mechanism as illustrated in Fig. 1.1, where a point electrical charge q is shown moving uniformly with velocity v , crossing the boundary at $y = 0$ between two different PhCs sharing the same crystal lattice, and exciting two counter-propagating edge states. Alternative configurations are described in Supplemental Material, including the excitation of guided modes of a linear defect inside a PhC. For simplicity, we focus on two-dimensional (2D) PhCs that do not rely on a photonic bandgap (PBG) for their confinement in the z dimension, but most of the results can be generalized to 3D. We further assume that the PhCs are non-magnetic and lossless.

Because the structure is still periodic in the x (albeit not in the y) direction, we choose an expanded "supercell" of the photonic structure comprised of one unit cell (of either PhC) in x and infinitely many in y direction. The supercell is used to compute the 1D Bloch states $\mathbf{E}_{k,n}(\mathbf{r}) = \mathbf{u}_n(k, \mathbf{r}) \cdot \exp(ikx)$, where the supercell's normalized x -periodic eigenmodes \mathbf{u} are characterized by their band number n , wavenumber k along the interface, and eigenfrequency $\omega_n(k)$. The eigenmodes can be sub-divided into two classes: (i) projected [38] bulk (extended) modes that have oscillatory behavior in y , and (ii) edge modes that exponentially decay as $e^{-\kappa|y|}$ away from the domain wall at $y = 0$, where $\kappa^{-1}(\omega)$ is the localization distance. The focus of our calculation is on the edge modes that occupy all, or part, of the common bandgap of the two PhCs: $\omega_{\text{lb}} < \omega < \omega_{\text{ub}}$, where $\omega_{\text{l(u)b}}$ are the lower

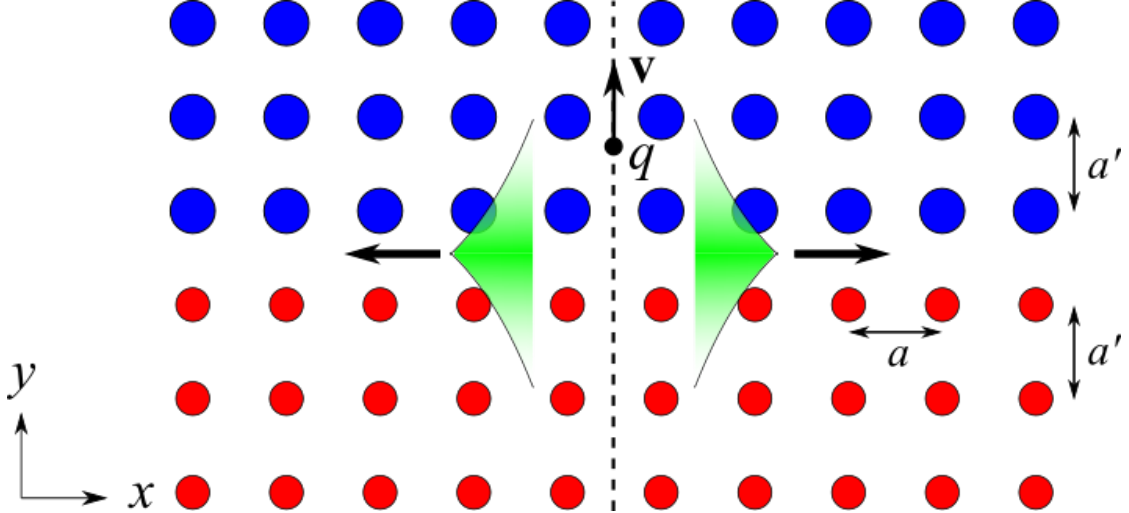


Figure 1.1: A schematic of transition radiation by a point charge at the interface of two photonic crystals. The charge moves from one PhC (small/red circles) to another (large/blue circles) with constant velocity v . Guided (edge) modes (green shades) propagating in the x direction are excited with frequencies inside the shared bandgap of the two PhCs , as well as bulk modes (not shown) at frequencies outside the bandgap. The period a along x direction and the lattice period a' along the beam's path are labelled.

(upper) bandgap edges.

The radiated electric field is calculated by solving the wave equation in the frequency domain: $\nabla \times (\nabla \times \tilde{\mathbf{E}}(\mathbf{r}, \omega)) = (\omega/c)^2 \epsilon(\mathbf{r}) \tilde{\mathbf{E}}(\mathbf{r}, \omega) + i\omega\mu_0 \tilde{\mathbf{J}}(\mathbf{r}, \omega)$, where $\epsilon(\mathbf{r})$ represents the inhomogeneous dielectric permittivity of the entire structure, and $\tilde{\mathbf{J}}(\mathbf{r}, \omega) = q\hat{r}_{\parallel}\delta^2(\hat{\mathbf{r}}_{\perp})\exp(i\omega r_{\parallel}/v)$ is the current density produced by the charge moving with the constant speed $\mathbf{v} = v\hat{r}_{\parallel}$ in the direction of $\hat{r}_{\parallel} = \mathbf{v}/v$, $r_{\parallel} = \mathbf{r} \cdot \hat{r}_{\parallel}$, and $\mathbf{r}_{\perp} \perp \hat{r}_{\parallel}$ are the two remaining spatial dimensions.

In the case of a continuous medium on both sides of the boundary, the TR problem has been solved [27, 17] by stitching the analytically known solutions at the boundary. This approach is not workable in the case of PhCs because analytic solutions for the propagating waves cannot be obtained. However, the problem is simplified in the case of edge wave excitation due to the remaining periodicity

in the x direction. Briefly, using the Bloch eigenmodes of the supercell as the expansion basis [76], the driven electric field can be expressed as an integral over the 1st Brillouin zone

$$\tilde{\mathbf{E}}(\mathbf{r}, \omega) = q \sum_n \int_{\text{BZ}} \frac{dk}{2\pi\epsilon_0} \frac{i\omega c_n(k, \omega) \mathbf{E}_{k,n}(\mathbf{r})}{(\omega + i\gamma)^2 - \omega_n^2(k)}, \quad (1.1)$$

where the expansion coefficients $c_n(k, \omega)$ are given by an integral along the beam's path defined as $\mathbf{r} = r_{\parallel} \hat{\mathbf{r}}_{\parallel}$:

$$c_n(k, \omega) = \int_{-\infty}^{\infty} dr_{\parallel} (\mathbf{u}_n^*(k, \mathbf{r}) \cdot \hat{\mathbf{r}}_{\parallel}) e^{i(\omega/v - k \cos \theta)r_{\parallel}}, \quad (1.2)$$

where θ is the angle between the directions of the beam's velocity and of the interface between the two PhCs. The summation over n includes all modes (edge and bulk), and an infinitesimal γ is introduced to ensure causality.

Only a discrete set of edge modes contributes to far-field radiation at frequencies inside the common bulk bandgap, thus enabling the following asymptotic limit of Eq. (1.1) (see Supplemental Material) at $x \rightarrow +\infty$:

$$\mathbf{E}(\mathbf{r}, t) \approx \sum_{m+} \int_{\omega_{lb}}^{\omega_{ub}} \frac{d\omega}{v_{m+}^{(g)}} \frac{qC_{m+}\mathbf{u}_{m+}}{4\pi\epsilon_0} e^{i(k_{m+}x - \omega t)}, \quad (1.3)$$

where $m+$ is the discrete index for all forward-propagating edge modes, with their corresponding wave numbers $\{k_{m+}(\omega)\}$ determined from the edge mode's dispersion relation $\omega_{m+}(k) = \omega$ and satisfying the causality condition $v_{m+}^{(g)}(\omega) \equiv (dk_{m+}/d\omega)^{-1} > 0$. The frequency-dependent spectral amplitudes $C_{m+}(\omega)$ of the transition edge radiation (TER) are obtained by substituting the implicitly frequency-dependent Bloch eigenfunctions $\mathbf{u}_{m+}(k_{m+}, \mathbf{r})$ of the edge modes into Eq.(1.2): $C_{m+} \equiv c_{m+}(k_{m+}(\omega), \omega)$. The expression for the electric field propagating in the $x < 0$ direction is identical to Eq.(1.3), except that the contributing modes (labeled with $m-$ index) satisfy $v_{m-}^{(g)}(\omega) < 0$.

The power spectrum $P_{\pm}^{\text{TER}}(\omega)$ of the forward/backward TER, which is finite for all frequencies where edge modes exist, can now be calculated (see Supplemental Material):

$$P_{\pm}^{\text{TER}}(\omega) = \frac{q^2}{4\pi\epsilon_0} \sum_{m\pm} \frac{|C_{m\pm}|^2(\omega)}{v_{m\pm}^{(g)}(\omega)} \quad (1.4)$$

This intuitive expression for the spectral power of edge waves, which is applicable to both continuous (see Supplemental Material for the application of this formalism to SPP generation [27, 17]) and photonic media, constitutes the main general result of this work.

1.2.1 Formation Length

One important concept in TR is the length L_f of the formation zone, based on the fact that radiation is not formed at a point but within a finite region [27]. In bulk TR, it is usually defined as the distance where the interference of the charge field and the radiation field is still important, and therefore determined by the phase difference of the two fields along the beam's path. Here for TER in PhCs, for simplicity, we discuss the case when $\theta = \pi$ (normal incident). The envelope of the charge field will have a phase dependence of $\omega y/v$; while the radiation field does not have phase variance along y direction, it exponentially decays away from the interface as $e^{-k|y|}$. The decay rate should play a role in the formation length L_f since if the edge mode is very localized, the charge can only interact with it in a short distance. Therefore it is reasonable to include both the phase difference and decay rate and define $L_f \sim |\omega/v + ik|^{-1}$ as the formation length.

1.3 Excitation of topological kink states

Next, we consider a specific example of kink states' excitation at the domain wall between two topologically-different PTIs shown in Fig. 1.2(a). The structure, based on Ref. [64], consists of two quantum spin-Hall (QSH) PTIs with opposite spin Chern numbers $C_s = \pm 1/2$. The QSH-PTIs are comprised of two parallel metal plates providing confinement in the z direction, patterned by a hexagonal lattice (of period a) arrangement of metal rods attached to either the top (right side of Fig. 1.2(a)) or the bottom (left side) metal plate. Its 1D-photonic band structure (PBS) and Bloch states are obtained using COMSOL eigenfrequency study. Fig. 1.2(b) shows the PBS, where black dots denote bulk modes, and colored solid lines inside the bandgap represent TPEWs.

The domain wall between two QSH-PTIs supports four TPEWs inside the bandgap: two forward and two backward TPEWs (two at each valley). The group velocities of the TPEWs are locked to their photonic spin [64]: spin-up ($m+$, red lines) modes propagate forward, while spin-down ($m-$, green lines) modes propagate backwards. For our specific design, the TPEWs span the shared topological bandgap bracketed by $\omega_{lb} = 0.72(2\pi c/a)$ and $\omega_{ub} = 0.77(2\pi c/a)$ from below and above, respectively. The TER-producing point charge is assumed to be moving along one of the high-symmetry axes of the hexagonal lattice, drawn through the mid-plane between the two metal plates and half-way between two adjacent rows of rods for optimal clearance. Therefore, the charge is crossing the domain wall between the two QSH-PTIs at the $\theta = \pi/3$ angle (see Fig. 1.2(a)), and is experiencing a periodic environment on both sides of the interface.

The choice of this specific photonic platform is dictated by its several unique properties. First, the supported TPEWs can be guided along sharply curved tra-

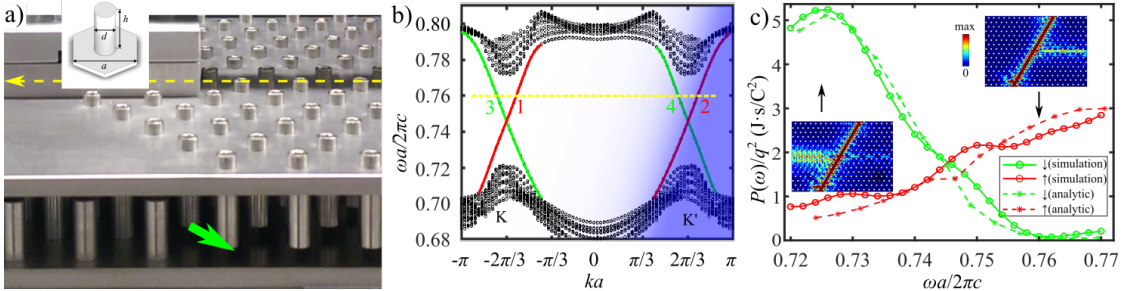


Figure 1.2: (a) Fabricated photonic structure comprised of two QSH-PTIs separated by the domain wall. The charge travels in the mid-plane between the plates under the dashed yellow line. The spin-down waves (green arrow) will be received at one end of the interface (spin-up waves not shown). Inset: unit cell geometry with realistic dimensions: $a=11.5$ mm, $d=3.97$ mm, $h=9.78$ mm. (b) The 1D PBS of the structure, projected onto the x axis. Black dots: bulk modes continua separated by the bandgap. Red/green solid lines: TPEWs with up/down (m_+/m_-) spins inside the bandgap. Horizontal dashed line: constant-frequency line intersecting the four TPEWs at different values of $k_{m\pm}(\omega)$. Blue shaded area: the ‘‘strong excitation belt’’. (c) The emitted TER inside the bandgap calculated from the analytic expression (Eq. (1.4), dashed lines) and *ab initio* simulation (solid lines). Red/green lines: TER to the right/left of the crossing point. Insets: the norm of the in-plane Poynting vector perpendicular to the beam’s path $|S_\perp|$ obtained from the simulation, at frequencies labeled by the black arrows. The beam moves form the lower to the upper PTI domain, and its trajectory is covered by over-saturated red. The horizontal PTI interface is located in the middle of the plot, below/above which rods are attached to the top/bottom plate.

jectories [64, 50, 44, 14] after their excitation. Second, the specific geometry of QSH-PTIs is conducive to its interaction with high-power electromagnetic radiation. That is because the transverse confinement of the kink states does not require any side walls, and because the attachment of the rods to just one metal plate enables their easy monolithic fabrication. Third, the sparsity of the QSH-PTI structure and the existence of clear passages for the charged beam along multiple unobstructed directions prevent a direct impact of electrons on the structure. We note that it has been recently shown in theory that unidirectional edge states can be predominantly excited by Cherenkov emission using magnetized plasmas or Weyl semi-metals [73].

The expression for the power spectrum $P_{\pm}^{\text{TER}}(\omega)$ involves 4 TPEWs that are graphically shown as the crossing points between the yellow dashed (constant frequency) line and the dispersion relations (solid lines) of the TPEWs in Fig. 1.2(b). These crossings are labeled as follows: $m = 1, 2$ crossings belong to $\{m+\}$ (spin-up TPEWs in the K/K' projected valleys), while $m = 3, 4$ correspond to their spin-down counterparts. The group velocities of all 4 TPEWs are approximately equal and constant across the bandgap: $v_m^{(g)}(\omega) \approx 0.4c$. The predicted spectra are plotted in Fig. 1.2(c) for the right/left-propagating TPEWs (dashed red/green lines), and are found in good agreement with *ab initio* driven simulation (solid lines), where $\tilde{\mathbf{J}}(\mathbf{r}, \omega)$ is implemented as the current source.

The TER spectra exhibit several notable features. First, we find that TER can be highly directional and spin-polarized: see the insets in Fig. 1.2(c) corresponding to $\omega_{\downarrow} \approx 0.725(2\pi c/a)$ (predominantly backward spin-down radiation), and to $\omega_{\uparrow} \approx 0.76(2\pi c/a)$ (forward spin-up radiation). On the other hand, for other frequencies at the center of the bandgap both forward and backward TPEWs of similar intensities are launched. Second, excitation of K valley TPEWs ($m = 1, 3$) is negligible compared with excitation of their K' valley ($m = 2, 4$) counterparts (see Fig. S2 in Supplemental Material for the spectra of all 4 TPEWs). Therefore, transition radiation mechanism provides a new way of valley-polarized excitation of TPEWs, and provides an opportunity to introduce the concept of quasi-phase matching (QPM) between charges and radiation.

The essence of QPM is that under the envelope function approximation [5], TPEWs are constructed from bulk modes of the 2D-periodic PhC with imaginary k_y^{bulk} (for the QSH-PTI we used, the edge mode with 1D wavevector k is constructed from bulk modes with purely imaginary $k_y^{\text{bulk}} = \pm ik \approx \pm 0.38ia^{-1}$ and real $k_x^{\text{bulk}} =$

$k \pm 2\pi/a$ for $K(k < 0)$ and $K'(k > 0)$ valley, respectively, due to band folding [65]), and for weakly confined-TPEWs, the projection of the real part of the 2D wavevector \mathbf{k}^{bulk} onto the charge trajectory must approximately match the wavenumber ω/v of the line current (or differ by a reciprocal vector) in order to get large overlap integral Eq. (1.2). Quantitatively, strong excitation of an edge mode is possible when its ω and k_x^{bulk} satisfies

$$|\omega/v - k_x^{\text{bulk}} \cos \theta + 2\pi N/a'| \lesssim \kappa \sin \theta, \quad (1.5)$$

for some integer N , where a' is the period along the beam's path. Note that in the limit of $\kappa \sin \theta \rightarrow 0$, we recover the so-called generalized Cherenkov condition [47]. We refer to the region defined by Eq. (1.5) as "strong excitation belt", and it is graphically represented in Fig. 1.2(b) as the blue shaded area ($N = -1$ for K' valley and $a' = a$). It's clear that only TPEWs at K' valley fall into this belt, and this explains why they are predominantly excited. One can also see the reason why the backward-moving TPEW 4 is excited much stronger at the lower edge of the bandgap than at the upper edge: its dispersion line lies deep inside the belt at lower frequencies but outside at higher frequencies. Additional examples corresponding to a sub-relativistic beam with $v = 0.56c$ (strong excitation belt covering K valley modes) and $v = 0.75c$ (no excitation), as well as detailed derivation of Eq. (1.5) are presented in Supplemental Material. The total emitted energy in the topological bandgap versus v is also plotted, where multiple sharp peaks correspond to significantly enhanced TER when the QPM condition is satisfied. QPM is important when (i) the edge mode can be well described by decaying bulk modes and (ii) the wave decay constant κ satisfies $\kappa a' \sin \theta \ll 2\pi$. Note that, formally, the QPM condition resembles the relationship between the emission angle θ and the frequency ω of the Smith-Purcell radiation produced by a charge moving along a periodic structure [94, 41]. The key differences in the case of TER considered by

us are as follows: (i) radiation is coupled into a discrete set of edge states, not into a bulk continuum, (ii) the emission angle θ is fixed by the relative orientations of the charge trajectory and the interface, and (iii) due to the transient nature of TER, the QPM condition is an inequality rather than a strict equation.

1.4 Experimental Validation

The experimental validation of the TER concept was carried out at the Argonne Wakefield Accelerator Facility (AWA-ANL) using a high-charge relativistic point-like electron beam ($q \sim 3$ nC, $E_b \approx 65$ Mev, and $\tau_b \approx 3$ ps) and a photonic structure that was modeled above. As sketched in Fig. 1.2(a), the bunch (yellow dashed line) traverses the interface between the two QSH-PTI domains near the center of the structure and excites TPEWs around the frequency of $f_0 \equiv \omega_0/2\pi \approx 19.5$ GHz. The fully-assembled structure is pictured in Fig. 1.3(a) inside a vacuum chamber. The objectives were to experimentally demonstrate the following: (a) unobstructed charged bunch propagation over many periods of the PhC along one of its principal directions under full vacuum; (b) the capability of the TR mechanism to exciting TPEWs inside the bulk bandgap, and (c) spatial localization of TPEWs close to the domain wall. The PhC was comprised of 15×13 unit cells, and its dimensions listed in the caption of Fig. 1.2 ensure a topological PBG in the $19 < f < 20$ GHz range (where $f = \omega/2\pi$).

For diagnosing the TER produced by the bunch, two probes were positioned along the outer edge of the structure to detect spin-down waves: one very close (Probe 1), the other (Probe 2) 6 periods away from the interface (see Supplemental Material for their exact positions). The comparison between the signals from the

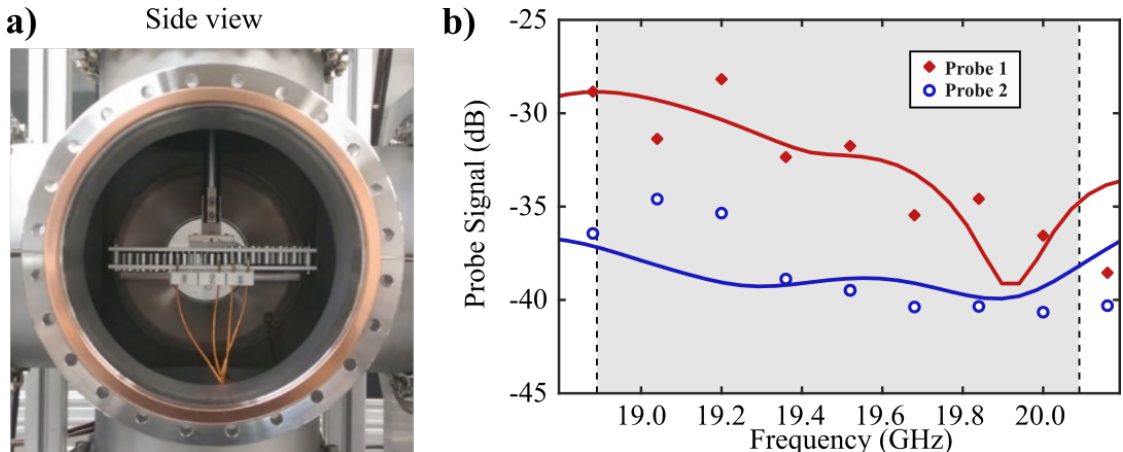


Figure 1.3: Experimental demonstration of transition edge-wave radiation (TER) using two interfaced QSH-PTIs. (a) fabricated structure inside the chamber. (b) Experimentally measured signals by Probe 1 (red diamonds) and 2 (blue circles). Numerical prediction: solid red (blue) curves for Probe 1 (2). Shadowed area: photonic bandgap, where only TPEWs exist.

two probes (see Fig. 1.3(b)) is used to demonstrate spatial localization of the EM energy at the interface. Indeed, the measured signal from Probe 1 (red diamonds) is much stronger than that from Probe 2 (blue circles) for every frequency inside the PBG (shadowed area). This contrast, which approaches 10 dB for some of the frequencies, implies that the beam excites edge waves. Topological protection of such modes has been demonstrated earlier [50] using antenna excitation. To our knowledge, this is the first time that TPEWs were shown to be excited via the TR mechanism. Due to limitation of the present experimental setup, we were only able to reliably measure signals at one end of the interface. Nonetheless, the measured result captures the most salient features predicted by our theory. For example, we see a clear trend of the TER decreasing in power as the frequency increases from the lower to the upper edge of the PBG. This is a consequence of the breakdown of the QPM near the upper edge of the PBG, as predicted by numerical simulation (solid red curve) and discussed above. Although the CR produced by the beam outside of the bandgap is beyond the scope of this Letter,

we note that the frequency positions (at 16 GHz and 18 GHz) of its two measured spectral peaks are also in good agreement with simulations results. Additional experimental and data processing details can be found in Supplemental Material. Future improvement of the experiment includes measuring spin-down waves and using a long train of electron bunches.

1.5 Conclusions

The TER concept can be used for beam diagnostics in the same way as TR of bulk waves because $P_{\pm}^{\text{TER}}(\omega)$ strongly depends on the beam's energy, duration, and the location of its trajectory. Novel beam-driven accelerators, such as matrix [89] and two-beam accelerators (TBAs) [43], and accelerators with a photonic-band-bap structure [81] can also benefit from TER. For example, possible geometries of a TER-based non-collinear (but parallel) TBA and a matrix accelerator are shown in Supplemental Material.

1.6 Supplemental Material

1.6.1 Some other configurations using TR to excite guided modes

As mentioned in the main text, the formalism of guided waves excitation by transition radiation we present is quite general and can be applied to many configurations other than the one shown in the Fig. 1, where kink modes between two different

PhCs are excited. One common example is shown in Fig. 1.4(a), where a charge

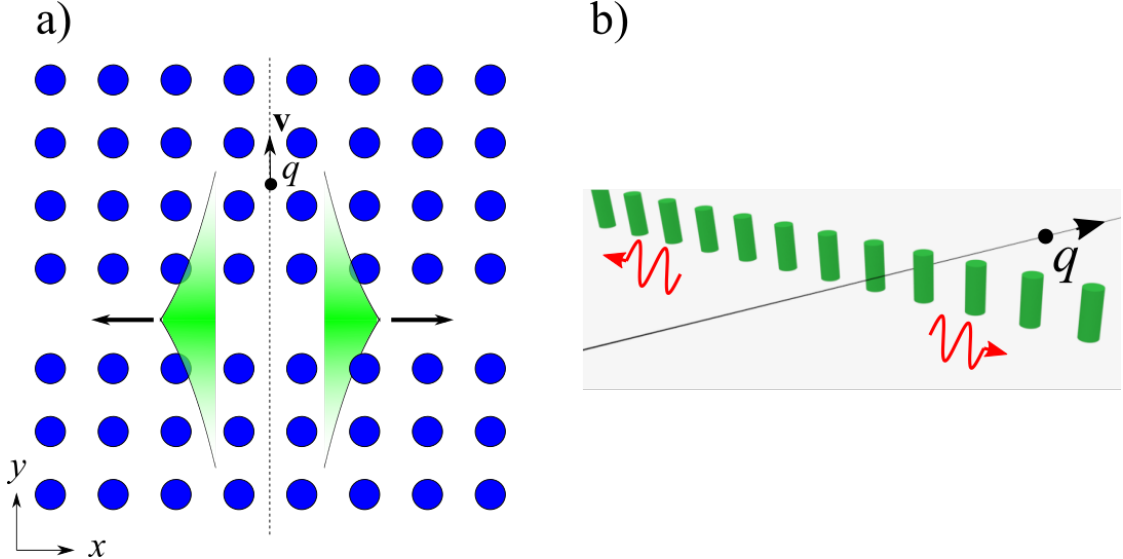


Figure 1.4: Some other configurations using TR to excite guided modes. (a) a charge crossing a linear defect in a PhC can excite the waveguide modes localized at the defect. (b) a charge moving closely past an array of rods forming a “periodic dielectric waveguide” [38], will also excite guided modes.

crossing a linear defect (for example, removing a row of rods) in a PhC can excite the waveguide modes localized at the defect. Another interesting example is shown in Fig. 1.4(b), where a charge moving closely past an array of dielectric rods, which forms a so-called “periodic dielectric waveguide” [38], will excite these guided modes. This configuration is interesting because here the difference between TR and diffraction radiation becomes fuzzy, since in a PhC it’s hard to tell whether the charge actually penetrates the structure.

1.6.2 Asymptotic behavior of electric field

First, for the sake of completeness of derivation, we mention here how the eigenmodes are chosen. The eigenmodes used to perform the expansion satisfy the

homogeneous wave equation (i.e., where $\mathbf{J} = 0$) and the following orthogonality/normalization conditions:

$$\int d^3r \epsilon(\mathbf{r}) \mathbf{E}_{k,n}^*(\mathbf{r}) \cdot \mathbf{E}_{k',n'}(\mathbf{r}) = 2\pi \delta_{nn'} \delta(k - k'). \quad (1.6)$$

Now we derive the asymptotic behavior of electric field far away from the source (where the charge cross the boundary): in Eq. (1), when $|x|/a \rightarrow \infty$ but y remains finite, both $c_{k,n}$ and $\mathbf{u}_{k,n}(\mathbf{r})$ are mathematically well-behaved. If $x > 0$, we can close the curve in Eq. (1) in the upper-half of the complex k -plane, and use the fact that the integral along the semicircle vanishes as $x \rightarrow \infty$ by Jordan's lemma. Using the residue theorem, we obtain:

$$\begin{aligned} & \int_{-\pi/a}^{\pi/a} \frac{dk e^{ikx} c_{k,n} \mathbf{u}_{k,n}(\mathbf{r})}{(\omega - \omega_{k,n} + i\gamma)(\omega + \omega_{k,n} + i\gamma)} \\ &= 2\pi i \sum_{m+} \left. \frac{c_{k,n} \mathbf{E}_{k,n}(\mathbf{r})}{-2\omega \cdot d\omega/dk} \right|_{k=k_{m+}}, \end{aligned} \quad (1.7)$$

where, for the ω residing in one of the common bandgaps, $\{k_{m+}\}$ are solutions of equation $\omega_{k,n} = \omega$ that simultaneously satisfy the causality condition $v_g := d\omega/dk > 0$ (i.e. energy propagates from the $x = 0$ point where the beam crosses the boundary to $x > 0$). Naturally, the causality requirement for $x < 0$ is $d\omega/dk < 0$.

1.6.3 Some useful identities of Bloch eigenmodes

In this sections we prove two useful identities of Bloch eigenmodes, which will be used in the next section.

First, in a lossless media, modes associated with different k , $(\mathbf{E}_1, \mathbf{H}_1)$ and $(\mathbf{E}_2, \mathbf{H}_2)$ are orthogonal in the sense that $\int d\mathbf{S} \cdot \Re[\mathbf{E}_1 \times \mathbf{H}_2^* + \mathbf{E}_2 \times \mathbf{H}_1^*] = 0$. To show this, note that since they are solutions of the homogeneous Maxwell solution,

we have

$$\begin{aligned} 0 &= \mathbf{E}_1 \cdot (\nabla \times \mathbf{H}_2^* - i\omega \mathbf{D}_2^*) \\ &= -\nabla \cdot (\mathbf{E}_1 \times \mathbf{H}_2^*) - i\omega (\mathbf{E}_1 \cdot \mathbf{D}_2^* - \mathbf{B}_1 \cdot \mathbf{H}_2^*). \end{aligned} \quad (1.8)$$

Therefore

$$\begin{aligned} &\nabla \cdot (\mathbf{E}_1 \times \mathbf{H}_2^* + \mathbf{E}_2 \times \mathbf{H}_1^*) \\ &= -i\omega (\mathbf{E}_1 \cdot \mathbf{D}_2^* - \mathbf{B}_1 \cdot \mathbf{H}_2^* + \mathbf{E}_2 \cdot \mathbf{D}_1^* - \mathbf{B}_2 \cdot \mathbf{H}_1^*). \end{aligned} \quad (1.9)$$

In a lossless media, the last line is purely imaginary, so $\Re[\nabla \cdot (\mathbf{E}_1 \times \mathbf{H}_2^* + \mathbf{E}_2 \times \mathbf{H}_1^*)] = 0$.

Now integrate this term in a unit cell and convert it to surface integrals

$$\begin{aligned} 0 &= \int_{x=x_0} d\mathbf{S} \cdot \Re[\mathbf{E}_1 \times \mathbf{H}_2^* + \mathbf{E}_2 \times \mathbf{H}_1^*] - \int_{x=x_0+a} d\mathbf{S} \cdot \Re[\mathbf{E}_1 \times \mathbf{H}_2^* + \mathbf{E}_2 \times \mathbf{H}_1^*] \\ &= (1 - e^{i(k_1 - k_2)a}) \int_{x=x_0} d\mathbf{S} \cdot \Re[\mathbf{E}_1 \times \mathbf{H}_2^* + \mathbf{E}_2 \times \mathbf{H}_1^*], \end{aligned} \quad (1.10)$$

where we have used the fact that the eigenmodes are edge modes so there is no power outflow in the y direction. Since $k_1 \neq k_2$ and they are restricted in the first Brillouin zone, the prefactor is non-zero. This proves the orthogonal relation we want.

Second, if we use only one mode in Eq. (1.10) instead of two different ones, then the first term vanishes because of periodicity, and we immediately see that electric energy equals the magnetic energy for any eigenmodes.

1.6.4 Derivation of the expression of energy spectral density

Since the total energy U emitted in the process of transition radiation is finite, we can use the energy spectral density $P(\omega)$, defined as

$$U = \int d\omega P(\omega), \quad (1.11)$$

to describe its spectral distribution. As discussed above, we only discuss frequencies in the bulk bandgap.

It can be easily shown (see Appendix A of Ref. [47] for a similar proof) that

$$P(\omega) = \frac{2}{\pi} \int d\mathbf{S} \cdot \frac{1}{2} \Re[\mathbf{E}(\mathbf{r}, \omega) \times \mathbf{H}^*(\mathbf{r}, \omega)], \quad (1.12)$$

where the integral surface S is the yz plane perpendicular to the direction of the energy flow, and located at large values of x (i.e. far from the crossing point).

Using the “orthogonal” property we proved in the last section, we see all the cross terms vanish, and the energy spectral density in $+x$ direction is

$$P(\omega) = \frac{2q^2}{\pi(2\epsilon_0)^2} \sum_{m+} \left. \frac{|c_k|^2 P_k}{v_g^2} \right|_{k=k_{m+}}, \quad (1.13)$$

where P_k is the power flow of a single mode calculated as

$$P_k = \int d\mathbf{S} \cdot \frac{1}{2} \Re[\mathbf{E}_k \times \mathbf{H}_k^*]. \quad (1.14)$$

Using the fact we just proved that electric energy equals the magnetic energy for any eigenmodes, and that the group velocity equals the energy transport velocity for a lossless mode [38], we further simplify the previous equation:

$$P_k = \frac{1}{4} \epsilon_0 v_g \times 2, \quad (1.15)$$

since the normalization condition in this case is

$$\int dy \int dz \int_0^a dx \epsilon(\mathbf{r}) |\mathbf{E}_k(\mathbf{r})|^2 = a. \quad (1.16)$$

Substituting Eq.(1.15) into Eq.(1.13) yields

$$P(\omega) = \frac{q^2}{4\pi\epsilon_0} \sum_{m+} \left. \frac{|c_k|^2}{v_g} \right|_{k=k_{m+}}. \quad (1.17)$$

Changing the label from $m+$ to $m-$ expresses the energy spectral density in the $-x$ direction.

1.6.5 Emission of surface plasmon polaritons by transition radiation

When a charge crosses the boundary of two media with different ϵ , it will excite surface modes, called surface plasmon polaritons (SPPs). This is discussed in detail in Ginzburg's book [27], although the terminology of SPP is not used. Since our approach, based on the assumption of PhCs, is more general, it should give the same answer. We will demonstrate it here.

We assume that the metal is at $z < 0$, and dielectric at $z > 0$. The normalized eigenmodes are

$$\mathbf{E}_{\perp,\mathbf{k}} = A \exp(\pm z \sqrt{k^2 - \epsilon \omega_k^2/c^2}) \hat{\mathbf{k}}, \quad (1.18)$$

$$E_{z,k} = \pm \frac{k}{\sqrt{k^2 - \epsilon \omega_k^2/c^2}} A \exp(\pm z \sqrt{k^2 - \epsilon \omega_k^2/c^2}), \quad (1.19)$$

where

$$A^2 = \frac{2k|\epsilon_1\epsilon_2|^{1/2}}{|\epsilon_2^2 - \epsilon_1^2|}, \quad (1.20)$$

$$\omega_k^2 = \frac{(\epsilon_1 + \epsilon_2)k^2 c^2}{\epsilon_1 \epsilon_2}. \quad (1.21)$$

The plus sign in Eq. (1.19) is for the metal, which we will use subscript 1 to denote afterwards, and minus sign and subscript 2 for the dielectric.

Using the result (Eqs. (1, 2)) from the main manuscript, the Fourier component of the E_z field in the metal is

$$\begin{aligned}
E_{z,k,1}(\omega) &= \frac{-i}{(2\pi)^2} \frac{\omega}{\epsilon_0} \frac{E_{z,k,1}}{\omega^2 - \omega_k^2} \left(\int_{-\infty}^0 dz' E_{z,k,1} q e^{i\omega z'/v} + \right. \\
&\quad \left. \int_0^\infty dz' E_{z,k,2} q e^{i\omega z'/v} \right) \\
&= \frac{-iq}{(2\pi)^2} \frac{\omega}{\epsilon_0} \frac{1}{\omega^2 - \omega_k^2} \frac{2k|\epsilon_1\epsilon_2|^{1/2}}{|\epsilon_2^2 - \epsilon_1^2|} \epsilon_2 \times \\
&\quad \exp(z \sqrt{k^2 - \epsilon_1 \omega_k^2/c^2}) \times \\
&\quad \left(\frac{1}{\epsilon_1} \frac{1}{\sqrt{k^2 - \epsilon_1 \omega_k^2/c^2} + i\omega/v} + \right. \\
&\quad \left. \frac{1}{\epsilon_2} \frac{1}{\sqrt{k^2 - \epsilon_2 \omega_k^2/c^2} - i\omega/v} \right)
\end{aligned} \tag{1.22}$$

This result is not exactly the same to (2.20) and (2.28) in Ref. [27], but this is because here in the eigenmode expansion, we only take into account the surface mode. To get the exact field, one need to include bulk modes (extended modes in either media) as well, which actually form a continuum in the 1D dispersion diagram. But if we are mainly interested in surface waves ($\mathbf{r}_\perp \rightarrow \infty$ but z finite), in which case we should take $\omega \rightarrow \omega_\kappa$ (the so-called plasmon-pole approximation [23]), then the result becomes identical to that in Ref. [27].

1.6.6 Quasi-phase matching between edge modes and the current

The QSH-PTI used in the main text has a Kane-Mele Hamiltonian [64]. By performing an calculation similar to the one in Ref. [86], one can verify that edge modes only exist when the two sides have opposite signs of Δ_{em} (using quantities defined in Ref. [64], same below) and thus opposite spin-Chern numbers, get the edge mode dispersion $\Omega = v_D \delta k_x$ (Ω and δk_x are detuning frequency and wavevector from the Dirac point), and see that the edge modes with 1D wavevector k are constructed from bulk modes with with purely imaginary $k_y^{\text{bulk}} = \pm i\kappa$, $\kappa = \Delta_{em} \omega_D / v_D \approx 0.38a^{-1}$ and real $k_x^{\text{bulk}} = k \pm 2\pi/a$ for $K(k < 0)$ and $K'(k > 0)$ valley, respectively. The additional term $\pm 2\pi/a$ is due to band folding when going from 2D Brillouin zone to 1D [65]. So the electric field of edge modes can be written as (subscript n is not written out for conciseness)

$$\mathbf{E}_k(\mathbf{r}) = \mathbf{u}'_k(\mathbf{r}) e^{ik_x^{\text{bulk}} x} e^{-\kappa|y|}. \quad (1.23)$$

Here $\mathbf{u}'(\mathbf{r})$ is a periodic function on a unit cell. Using this expression, and note that $y = r_{\parallel} \sin \theta$, Eq. (2) would become

$$c(k, \omega) = \int_{-\infty}^{\infty} dr_{\parallel} (\mathbf{u}'_k^*(\mathbf{r}) \cdot \hat{r}_{\parallel}) e^{i(\omega/v - k_x^{\text{bulk}} \cos \theta)r_{\parallel} - \kappa \sin \theta |r_{\parallel}|}. \quad (1.24)$$

Now that $\mathbf{u}'_k^* \cdot \hat{r}_{\parallel}$ is a periodic function with periodicity a' , we can expand it as a Fourier series: $\mathbf{u}'_k^* \cdot \hat{r}_{\parallel} = \sum_{N=-\infty}^{\infty} c_N(k) e^{2\pi i N r_{\parallel}/a'}$. Then the spectral amplitude (subscript

$m\pm$ is not written out for conciseness)

$$\begin{aligned}
C(\omega) \equiv c(k(\omega), \omega) &= \sum_{N=-\infty}^{\infty} c_N(k(\omega)) \int_{-\infty}^{\infty} dr_{\parallel} e^{i(2\pi N/a' + \omega/v - k_x^{\text{bulk}}(\omega) \cos \theta)r_{\parallel} - \kappa \sin \theta |r_{\parallel}|} \\
&= \sum_{N=-\infty}^{\infty} c_N(k(\omega)) \int_0^{\infty} dr_{\parallel} \{ e^{[i(2\pi N/a' + \omega/v - k_x^{\text{bulk}}(\omega) \cos \theta) - \kappa \sin \theta]r_{\parallel}} \\
&\quad + e^{[-i(2\pi N/a' + \omega/v - k_x^{\text{bulk}}(\omega) \cos \theta) - \kappa \sin \theta]r_{\parallel}} \} \\
&= \sum_{N=-\infty}^{\infty} c_N(k(\omega)) \left[\frac{1}{-i(2\pi N/a' + \omega/v - k_x^{\text{bulk}}(\omega) \cos \theta) + \kappa \sin \theta} \right. \\
&\quad \left. + \frac{1}{i(2\pi N/a' + \omega/v - k_x^{\text{bulk}}(\omega) \cos \theta) + \kappa \sin \theta} \right] \\
&= \sum_{N=-\infty}^{\infty} c_N(k(\omega)) \frac{2\kappa \sin \theta}{(2\pi N/a' + \omega/v - k_x^{\text{bulk}}(\omega) \cos \theta)^2 + (\kappa \sin \theta)^2}. \tag{1.25}
\end{aligned}$$

is the sum of a series of Lorentzian-like functions, assuming the Fourier coefficients $c_N(k)$ are slow varying functions of k , since $k(\omega)$ has a approximately linear dependence on ω . If $\kappa a' \sin \theta \ll 2\pi$, the Lorentzian peaks will be well separated, and we can take the half width at half maximum as a criterion for strong excitation:

$$|\omega/v - k_x^{\text{bulk}}(\omega) \cos \theta + 2\pi N/a'| \lesssim \kappa \sin \theta, \tag{1.26}$$

or, if we define k_b as the value of k that lets the left hand side of the above inequality be zero for some integer N , this strong excitation condition can be expressed as

$$|k(\omega) - k_b| \lesssim \kappa \tan \theta. \tag{1.27}$$

Using the relation between k and k_x^{bulk} , we obtain the following formula for k_b for the $K-$ ($k < 0$) and K' -valley ($k > 0$) states, with $\theta = \pi/3$ and $a' = a$:

$$\omega = \frac{k_b v}{2} + \frac{2\pi c}{a} \left(N - \frac{1}{2} \right) \frac{v}{c} \quad \text{for } k > 0 \tag{1.28}$$

$$\omega = \frac{k_b v}{2} + \frac{2\pi c}{a} \left(N + \frac{1}{2} \right) \frac{v}{c} \quad \text{for } k < 0, \tag{1.29}$$

where both ω and v are assumed positive. Here, because of the specific choice of $\theta = \pi/3$, both valleys share the same series of k_b 's, but the value of N depends on which valley is referred to. These lines can be referred to as “beam lines”.

The inequality Eq. (1.27) will define a series of belts in the 1D PBS, which we shall refer to as “strong radiation belts”. For $v = c$, they are shown as the blue belts in Fig. 1.5(b), corresponding to $N = 1, 2$ in Eq. (1.28). Note that although the 1D PBS has a period of $2\pi/a$ and can thus be confined in the first Brillouin zone $-\pi/a < k < \pi/a$, the “strong excitation belts” do not (here they have a period of $4\pi/a$ instead), and k_b can go far beyond the first Brillouin zone. The underlying reason is that k_b is originated from the 2D PBS.

We note that the concept of the beam line introduced here to describe the most efficient excitation of the TR is fundamentally different from the much more familiar related concept of the $\omega_b^{\text{res}} = \mathbf{k} \cdot \mathbf{v}$ dispersion curve used in the context of the resonant (Cherenkov) radiation of electromagnetic waves. For example, in the context of Cherenkov excitation of TPEWs, one could use a beam co-propagating with the interface (e.g., in the x -direction), where the appropriate resonant beam dispersion can be expressed as $k = k_b^{\text{res}}(\omega) \equiv \omega/v$. Cherenkov radiation is excited at, and only at the frequencies ω^{res} such that the following equation is satisfied: $k_b^{\text{res}}(\omega^{\text{res}}) = k_n^{\text{TPEW}}(\omega^{\text{res}}) + 2\pi N/a$, where N is an integer. Applications of such resonant wave-particle interactions to high power generation has been considered in the context of beam-powered traveling-wave microwave tubes [85, 28] and, more recently, metamaterials and metawaveguides [78].

On the contrary, the transition radiation is not a resonant process. That’s why “strong excitation belt” is a more appropriate condition for strong excitation than the “beam line”. The condition Eq. (1.27) can be interpreted as “quasi-phase matching”: although the edge modes decay away from the interface, they can still be assigned a “quasi-wave vector” along the charge trajectory. If it approximately matches the wave vector ω/c of the line current, the overlap integral in Eq. (1.24)

becomes large, and the TPEW is strongly excited.

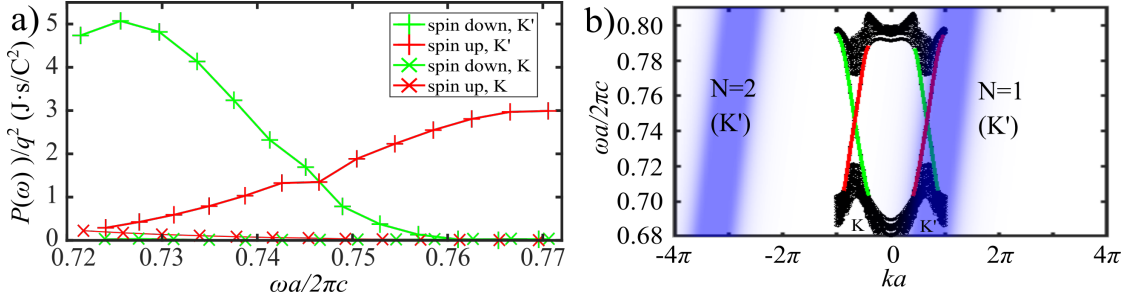


Figure 1.5: (a) The spin- and valley- specific energy spectral density with a charge of $v \approx c$, where it is clear that edge modes at K' valley is dominantly excited. (b) The 1D PBS of the supercell and the "strong excitation belts" in blue corresponding to Eq. (1.28) with $N = 1, 2$.

It is straightforward to apply this “quasi-phase matching” idea if we want to predominantly excite edge waves at the other valley. Simple calculation shows that changing v to $0.56c$ while keeping the trajectory satisfies Eq. (1.29) with $N = 1$, and Eq. (1.28) with N far from any integer. The resultant energy spectral density shown in Fig. 1.6(a) verifies our expectation, where both spin modes at K -valley is dominantly excited. The corresponding strong excitation belts are shown in Fig. 1.6(b).

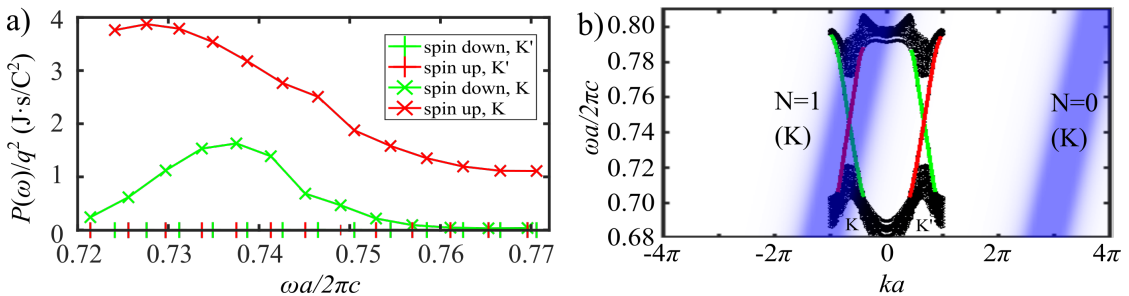


Figure 1.6: (a) The spin- and valley- specific energy spectral density with a charge of $v = 0.56c$, where it is clear that edge modes at K valley is dominantly excited. (b) The 1D PBS of the supercell and the “strong excitation belts” in blue corresponding to Eq. (1.29) with $N = 1, 0$.

If the quasi-phase matching condition is satisfied for neither valley (i.e. the strong radiation belts cover none of the 4 edge modes), then none of the modes will

be strongly excited. For example, if $v = 0.75c$ and the beam's path is unchanged (see the strong radiation belts in Fig. 1.7(b)), then for all 4 modes, $P(\omega)/q^2 < 0.1 \text{ J}\cdot\text{s}/\text{C}^2$ throughout the bandgap.

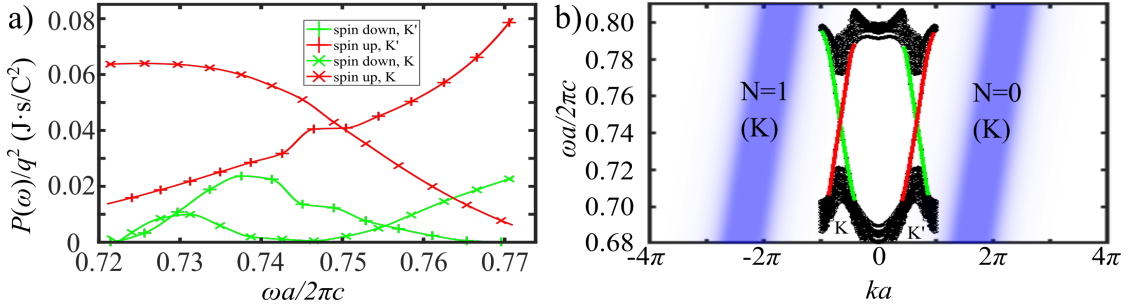


Figure 1.7: (a) The spin- and valley- specific energy spectral density with a charge of $v = 0.75c$, where it is clear that edge modes at neither valley is strongly excited. (b)The 1D PBS of the supercell and the strong radiation belts in blue corresponding to Eq. (1.29) with $N = 1, 0$.

The existence of strong QPM indicates that if one plots the total emitted energy in the topological bandgap $< 0.72\omega a/2\pi c < 0.77$ as a function of the speed of the charge v , there would be several peaks corresponding to QPM with different N 's. Fig. 1.8 confirms this, where three quite sharp peaks are evident. The valley-specific energies are also plotted so one can verify that two of the peaks correspond to QPM being satisfied for K' valley modes and one peak corresponds to QPM being satisfied at K valley. This relation between energy and speed of charge is drastically different from the case of excitation of SPPs by electron bombardment of a metal surface where integrated emission energy monotonously increase with electron energy [17]. The difference emphasizes the role of the lattice plays here, and it is also evident that the mechanism of QPM enhances the TER significantly in this platform.

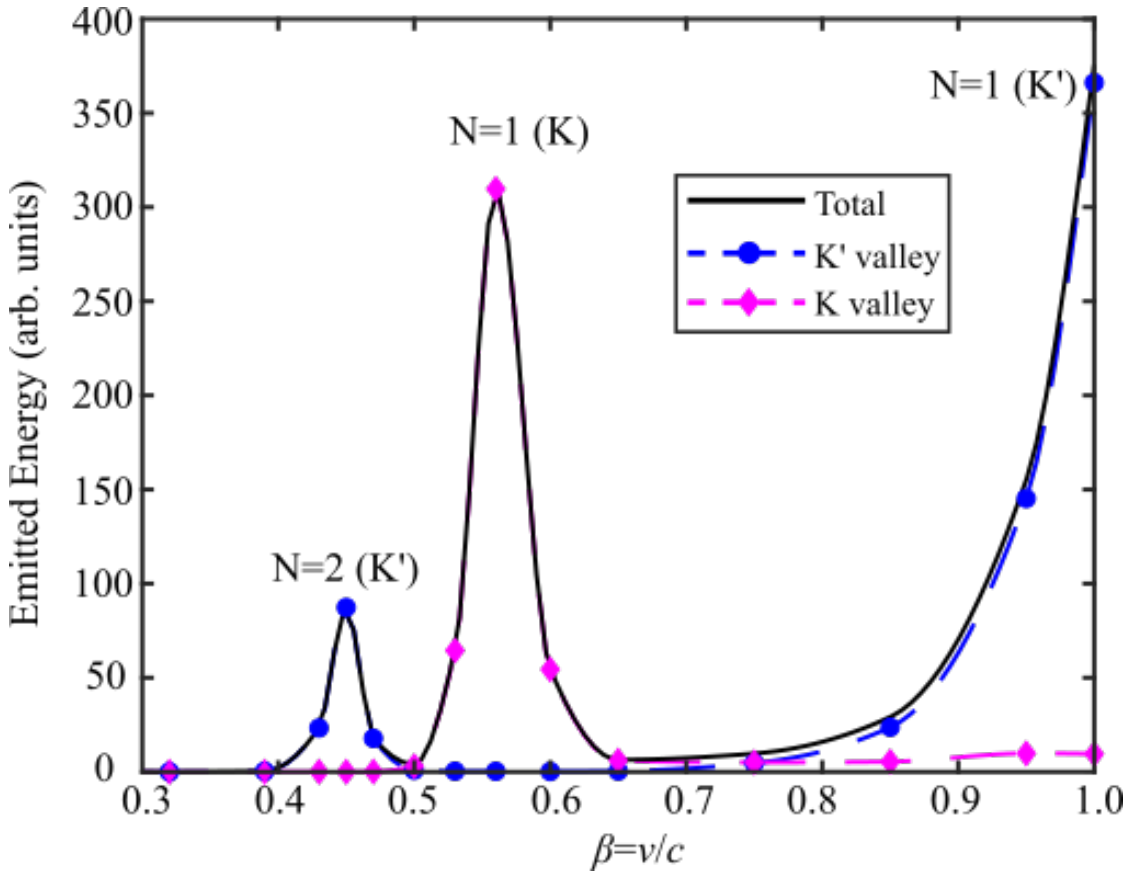


Figure 1.8: TER emitted energy in the topological bandgap $< 0.72\omega a/2\pi c < 0.77$ as a function of the speed of the charge v . Peaks are labelled by the value of N that satisfies in Eqs. (1.28) or (1.29) at that speed.

1.6.7 Experimental setup

The operating frequency of the QSH-PTI platform was designed to be around $f_0 = 19.5$ GHz. (15th harmonic of 1.3 GHz frequency of the photoinjector cavity), with the following geometrical parameters: $a_0 = 11.5$ mm, $d_0 = 3.97$ mm, $h_0 = 9.78$ mm as shown in inset of Fig. 1.9. The central operating frequency is chosen for two practical reasons: (i) to maintaining a sizable aperture for an electron bunch to propagate through the structure, and (ii) for the structure to be small enough for the installation into an existing vacuum chamber.

A platform consisting of 15×13 QSH-PTI unit cells is considered as the struc-

ture under test in this study. This choice of dimensions is a trade-off between limitations such as, available space in vacuum chamber, aperture clearance for electron transmission through structure, and sufficient number of PCs for pronounced collective behaviors. In Fig. 1.9, the structure is made of aluminum 6061

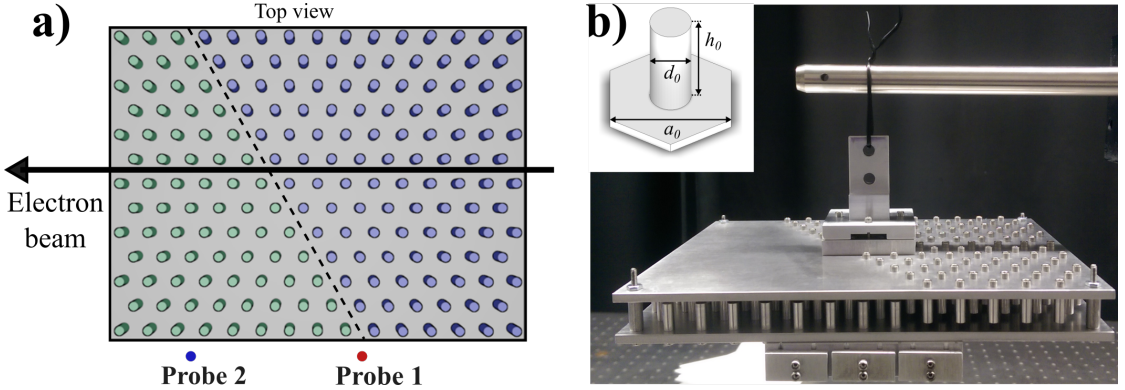


Figure 1.9: (a) Schematic of the 19.5 GHz structure composed of 15×13 QSH-PTIs. Domain with rod attached to the top (bottom) plate is colored in purple (green). Solid dots indicate the position of probes. (b) Fabricated structure with cable holder and counterweight. Inset: geometrical parameters: $a_0=11.5$ mm, $d_0=3.97$ mm, $h_0=9.78$ mm.

with monolithic metal machining and is subsequently assembled with other parts using fasteners. RF probes modified from Kapton insulated soft coaxial cables (30AWG, 50Ω) are clamped by a cable holder and positioned on the longer edge of the structure to measure the edge wave excited by transition radiation of electron as shown in Fig. 5a. A counterweight is attached to the opposite side to render the whole assembly balanced. The electron beam tests were carried out in collaboration with Argonne Wakefield Accelerator Facility in Argonne National Laboratory (AWA in ANL). The structure under test was installed in a six-way cross vacuum chamber and mounted on an actuator. A 3 nC, 65 MeV electron bunch with 6 ps duration was delivered to the vacuum chamber. Charge measurement was taken by two beamline ICTs located both downstream and upstream to the chamber as shown in the Fig. 1.10(a). The incident charge and transmitted charge were

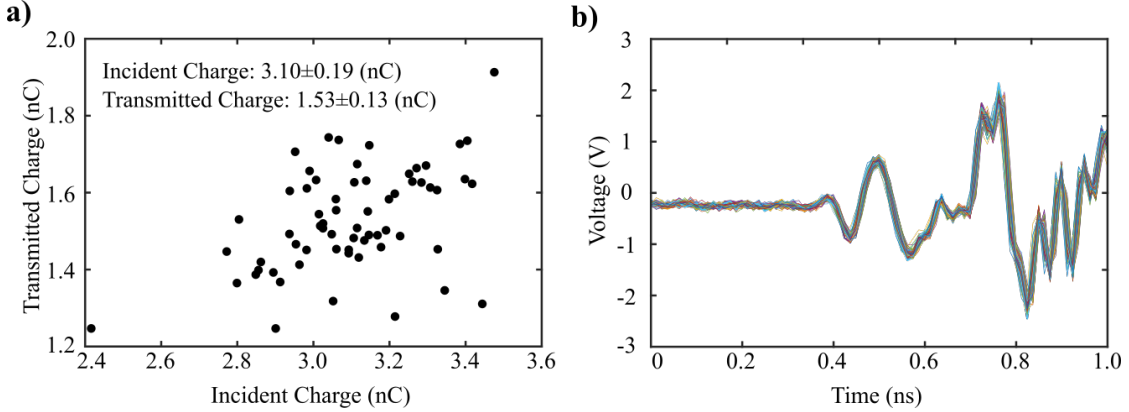


Figure 1.10: Charge and radio frequency measurement for the structure under test. (a) Charge measured by two ICTs on both upstream and downstream side of the experiment chamber. (b) Time domain alignment of acquired radio frequency signal. The figure contains 64 shots of measurements.

calculated as 3.10 ± 0.19 nC and 1.53 ± 0.13 nC respectively which corresponding to 49% transmission rate. A fast oscilloscope (Keysight DSAZ334A) with 4 channels, 80 GHz sampling rate, and 33 GHz bandwidth was employed to measure the RF signal in this experiment. In Fig. 1.10(b), data from 64 shots were aligned to each other in time domain to ease out shot-to-shot variation for data post-processing.

In the experiment we also measured two Cherenkov peaks outside but near this topologically non-trivial bandgap, at 16 and 18 GHz, respectively, shown in Fig. 1.11, as simulation predicts. This confirms our probes were working properly and were sensitive enough to pick up signals at this frequency regime.

1.6.8 TER-based accelerators

We first show a possible geometry of TER-based non-collinear two-beam accelerators in Fig. 1.12. It consists of alternative regions of SH-PTIs with rods attached to either the top plate (labeled \otimes) or the bottom plate (labeled \odot). Each time the

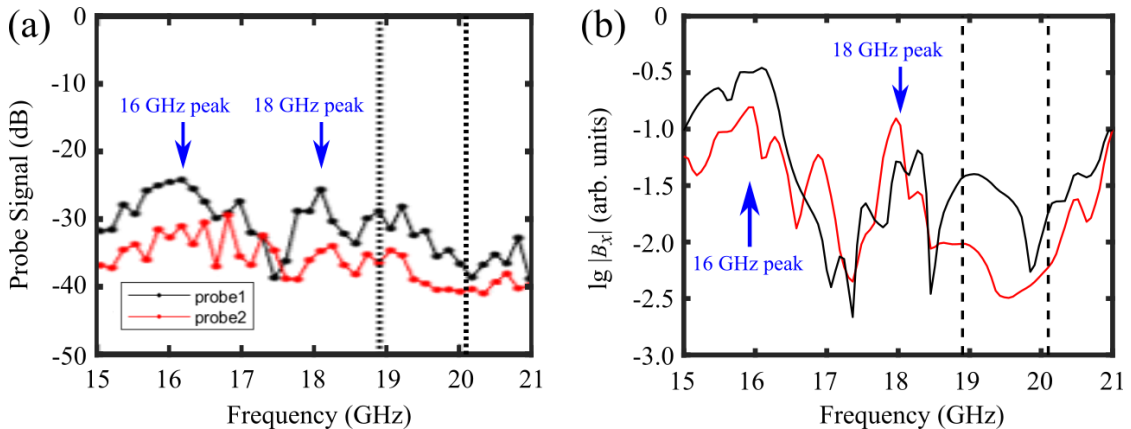


Figure 1.11: Experimentally measured (a) and simulated (b) signals by the two probes, in a wider frequency range 15 to 21 GHz. The two Cherenkov peaks predicted by simulation are clearly visible in the experimental data. Dashed lines mark the boundaries of the photonic bandgap.

drive beam crosses the interface, it will emit TER. The TPEW then propagate along the interfaces, and encounter the accelerated beam, giving it a boost. The accelerated beam does not travel along an interface, so one does not have to worry about synchronization between the beam and TPEWs [90], which turns out to be quite difficult. The introduction of TPEWs gives us the privilege to bend the interfaces in the “wave-propagating region”, without need to worry about reflection. In practice, a series of bunches with carefully chosen separation can be used to enhance the excitation at a desired frequency. Note according to Fig. 2 in the main text, it’s possible to dominantly excite only one spin by wisely choosing the operating frequency. When the driver beam reaches the next interface, by a simple argument of time-reversal symmetry ($\tilde{\mathbf{J}}(\mathbf{r}, \omega) \rightarrow -\tilde{\mathbf{J}}^*(\mathbf{r}, \omega)$, $\mathbf{E}_{k,n}(\mathbf{r}) = \mathbf{E}_{-k,n}^*(\mathbf{r})$, so $|c_n(k, \omega)| \rightarrow |c_n(-k, \omega)|$), it will dominantly excite the other spin. However, because of the type of interface also “flips”, the radiation still propagate in the same direction. Therefore, it is possible to make the majority of TER produced by the drive beam at every interface all goes towards the accelerated beam, thus increasing the efficiency.

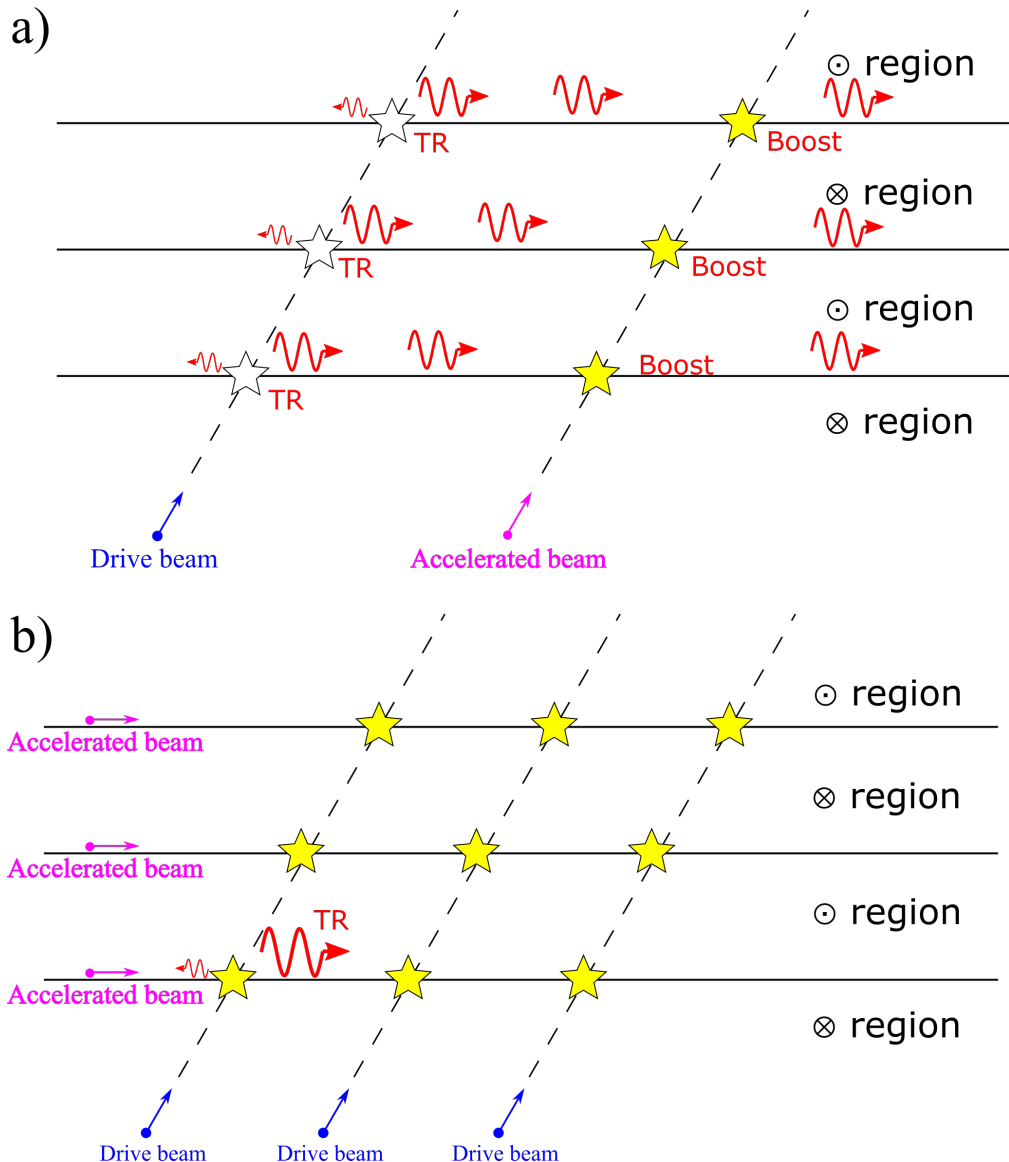


Figure 1.12: (a) A sketch of a TER based two-beam accelerator. It consists of alternative regions of SH-PTIs with rods attached to either the top plate (labeled \otimes) or the bottom plate (labeled \odot). Individual rods are not plotted. Each time the drive beam crosses the interface (white stars), it will emit TER. The TPEW then propagate along the interface (red arrows), and encounter the accelerated beam, giving it a boost (yellow stars). (b) A sketch of a TER based matrix accelerator.

Next we show a possible geometry of TER-based matrix accelerators in Fig. 1.12. The differences from the previous design are: (a) now there are multiple drive beams travelling parallel to each other, thus increasing the field strength; (b) the accelerated beams are not parallel to the drive beams, but instead each

travels along an interface; (c) multiple beams can be accelerated at the same time, increasing the overall energy usage efficiency. One challenge for this design is that the interface between two opposite spin-PTIs need to be carefully designed (for example introducing some detours), in order to achieve synchronization between the beam and TPEWs, and high acceleration.

CHAPTER 2

APPLICATION OF JORDAN DECOMPOSITION TO

NON-HERMITIAN LATTICE MODELS WITH

SPECTRALLY-ISOLATED LOWER DIMENSIONAL STATES

This Chapter was a modification of article [99], and was posted on arXiv [100].

2.1 Introduction

Non-Hermitian physics has attracted considerable interest in recent years because of its relevance to non-equilibrium (e.g., undergoing photo-ionization) systems [4, 62]. Some of its notable phenomena include “exceptional points” (EPs) [35, 10, 67] and real-valued spectra despite non-Hermiticity. At the EP, both the complex-valued eigenvalues of two bands as well as their corresponding eigenvectors coalesce [20, 18]. In other words, the matrix corresponding to the Hamiltonian at the EP becomes *defective* [29, 54]. The completely real spectrum of some non-Hermitian systems can be related to parity-time (PT) symmetry [8, 88, 9] or pseudo-Hermiticity [68], though in general it is hard to assert a real spectrum without directly calculating the eigenvalues.

In this paper we will focus on non-Hermitian lattice models, where the Hamiltonian of the system can be represented by a finite dimensional non-Hermitian matrix. There has been a considerable amount of literature on these systems recently [59, 54, 48, 96, 42, 61, 66, 77, 37]. However, most literature uses eigendecomposition, which is in fact only appropriate for Hermitian matrices [29]. This leads to at least two possible issues: (1) not identifying all approximate eigenstates of the system and (2) the eigenstates do not form a complete basis. To see why

(1) can happen, consider the following two-level Hamiltonian:

$$H = \begin{pmatrix} 0 & q_1^N \\ q_2^N & 0 \end{pmatrix}, \quad (2.1)$$

in the basis $\{|1\rangle, |2\rangle\}$, where $|q_2| < |q_1| < 1$ and $N \gg 1$ is the size of the system. The usual eigendecomposition would give the eigenstates of the system as $|1\rangle \pm (q_2/q_1)^{N/2}|2\rangle \approx |1\rangle$ when $N \rightarrow \infty$. However, in reality, the exponentially small off-diagonal terms q_1^N and q_2^N should not be compared against each other. Rather, they should be compared against some characteristic energy scale E_c of the system. If $|q_1|^N \ll E_c$, then states $|1\rangle$ and $|2\rangle$ are both good approximate eigenstates of the system. For example, if we observe the system on a time scale much shorter than $1/|q_1|^N$, then if the system starts in either state it will remain in that state during our observation. Likewise, if the system has some finite loss Γ , which is inevitable for any real-world passive systems, then $E_c \sim \Gamma$. A third scenario is when the states $|1\rangle$ and $|2\rangle$ have a small but finite energy split ϵ , which is also inevitable for realistic systems, then $E_c \sim \epsilon$. This example demonstrates that the eigendecomposition of non-Hermitian matrices can be numerically unstable and return pathological results. The second issue comes into play in the excitation of modes and can lead to the “missing dimension” [13].

There are many decomposition that are applicable to non-Hermitian matrices but the one most relevant to the physics community and will serve as the replacement for the eigendecomposition is the Jordan decomposition. This is because we are interested in solving the equation of motion (EOM) of the system: $i\psi/dt = H\psi + \xi$, either without a source ($\xi = 0$, homogeneous) or with a source ($\xi \neq 0$, inhomogeneous), which involves calculating the resolvent or exponential of the Hamiltonian, and the resolvent or exponential of a Jordan block is easy to calculate (this is also the primary reason why we use the eigendecomposition

for Hermitian matrices). For example, suppose we have a periodic source with frequency E , and the spectrum of the system is purely real (either because of PT symmetry or pseudo-Hermiticity), then adding a small overall loss Γ to the system ensures all transients eventually decay. Therefore, only the driven equation $(E - H + i\Gamma)\psi = \xi$ needs to be solved. If we obtain the Jordan decomposition of the Hamiltonian $H = PJP^{-1}$, we can instead solve $(E - J + i\Gamma)\psi' = \xi'$ where $\xi' = P^{-1}\xi, \psi = P\psi'$. We see we need to obtain both the relevant columns of P matrix and rows of P^{-1} corresponding to eigenvalues near E . We call the former right Jordan basis and the latter left Jordan basis, a generalization of right and left eigenvectors.

While it is known that Jordan decomposition is not numerically stable either, the Schur decomposition is [29]. After obtaining the Schur decomposition, one can group close eigenvalues together and obtain invariant subspaces. In practice this can be difficult for bulk continuum of the spectrum, but if there are lower dimensional modes that are isolated in the spectrum, this approach is straightforward. What we will get is a block diagonal form

$$H = P \begin{pmatrix} J_0 & 0 \\ 0 & J_r \end{pmatrix} P^{-1}, \quad (2.2)$$

where J_0 is a $n \times n$ upper diagonal matrix with grouped eigenvalues E_0 on the main diagonal. The explicit procedures are: (1) calculate the Schur decomposition: $H = UTU^\dagger$, and find isolated eigenvalues we are interested in; (2) order the Schur decomposition so that these eigenvalues appear first on the main diagonal of T , then the first block of T is J_0 , and the first n columns of U , $\eta_1^R, \dots, \eta_n^R$, are the first n columns of P ; (3) repeat the above steps on H^T , get the first columns of U (a different one) as $\eta_1^L, \dots, \eta_n^L$; (4) let $\Sigma = (\eta_1^L, \dots, \eta_n^L)^T(\eta_1^R, \dots, \eta_n^R)$, then $\Sigma^{-1}(\eta_1^L, \dots, \eta_n^L)^T$ are the first n rows of P^{-1} .

Next we use a non-Hermitian quadrupole insulator (QI) model from Ref. [59] as a nice example to demonstrate how Jordan decomposition comes in handy when analyzing the behavior of the system. This model is schematically shown in Fig. 2.1(a), where the intra/inter-cell hopping amplitudes $t \pm \gamma$ and λ are all taken to be real. It is a natural non-Hermitian generalization of the QI model described in Ref. [7], with the intracell hopping strength becoming asymmetric, characterized by a finite γ , while maintaining the sublattice symmetry $\Sigma H \Sigma^{-1} = -H$. Here the symmetry operator $\Sigma = P_1 - P_2 - P_3 + P_4$, where $P_j = \sum_{x,y} |x,y,j\rangle\langle x,y,j|$ are the sublattice projection operators, and $|x,y,j\rangle$ are the tight-binding states, where x and y are integer-valued coordinates of the unit cells as defined in Fig. 2.1(a), and $j = 1, \dots, 4$ denote four sub-lattice sites of each unit cell. This model can also be viewed as a two-dimensional (2D) generalization of the non-Hermitian Su-Schrieffer-Heeger (SSH) model [56, 98, 96].

2.2 Non-Bloch bulk continuum

As was pointed in the context of the non-Hermitian SSH system [96], the open-boundary spectrum can significantly differ from that of the periodic-boundary system described by the Bloch Hamiltonian $H(\vec{k})$. That is because the usual Bloch phase-shift factor e^{ik} for bulk eigenstates (i.e., eigenstates in the continuum spectrum) of an open-boundary system needs to be modified to $\beta \equiv \beta_0 e^{ik}$, where β_0 can be non-unity (i.e., the wavevector acquires an imaginary part: $k \rightarrow k - i \ln \beta_0$). This extra *bulk localization factor* β_0 must be taken into account when calculating the spectrum of the open-boundary system. The same argument applies to our 2D non-Hermitian QI system, where $\vec{k} \equiv (k_x, k_y) \rightarrow (k_x - i \ln \beta_0, k_y - i \ln \beta_0)$, and $\beta_0 = \sqrt{|(t - \gamma)/(t + \gamma)|}$ [59]. With this substitution, the corrected Bloch Hamiltonian

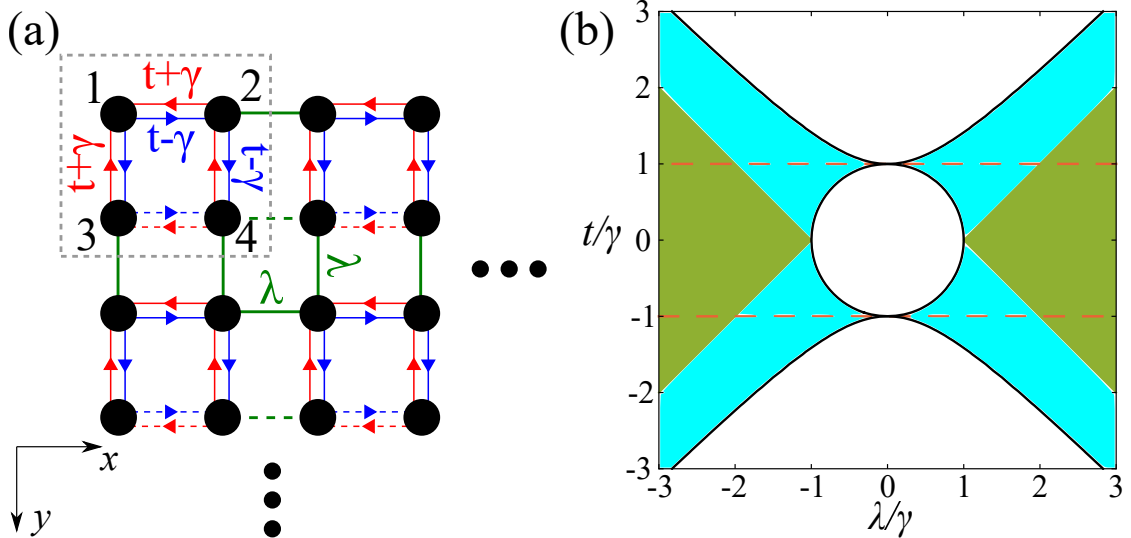


Figure 2.1: (a) Tight binding model of a non-Hermitian QI on a square lattice. Grey dashed line: boundary of unit cell with four (sublattice) sites (numbered 1 to 4). Red and blue lines with arrows: asymmetric intra-cell hopping amplitudes $\pm t \pm \gamma$, green lines: symmetric inter-cell hopping amplitudes $\pm \lambda$. Dashed lines: negative hopping terms. All four sublattices have the same on-site potentials (set to $\epsilon_j \equiv 0$). (b) The phase diagram of a large non-Hermitian QI with open boundary condition. Green region ($|\lambda| > |t| + |\gamma|$): near-Hermitian regime with 4 zero-energy corner states, each localized at a separate corner. Cyan region ($\sqrt{|t^2 - \gamma^2|} < |\lambda| < |t| + |\gamma|$): intermediate regime with 2 zero-energy corner states at the top-left corner. White region ($|\lambda| < \sqrt{|t^2 - \gamma^2|}$): no corner states. Bandgap vanishes along solid black lines. The spectrum is complex-valued between the two dashed orange lines, real-valued elsewhere.

shows (see the Supplemental Material) agreement with numerical simulations of an open-boundary system, that a finite bulk bandgap exists for all values of the hopping amplitudes except at $t^2 = \gamma^2 \pm \lambda^2$. The zero-gap condition is represented in Fig. 2.1(b) by the solid black lines.

Another important consequence of this extra factor β_0 is that the bulk spectrum is real-valued for $|t| > |\gamma|$. While there are also edge and corner states, our numerical results show that the entire spectrum is real for arrays of any size whenever $|t| > |\gamma|$. This fact can be related to the pseudo-Hermiticity of the Hamiltonian [59].

2.3 Zero-energy corner states

Having established the bulk properties of non-Hermitian QIs, we now proceed with investigating the properties of zero-energy corner states supported by a large ($N \times N$ array, $N \gg 1$) non-Hermitian QI with open boundary conditions, using Jordan decomposition. When the inter-cell hopping strength dominates over the intra-cell one, i.e. $|\lambda| > |t| + |\gamma|$, the system has zero as an eigenvalue of algebraic multiplicity four. The Schur form of this invariant subspace turns out to be approximately a diagonal matrix $J_0 = 0_{4 \times 4}$. Thus the left and right basis states in this case are all left/right eigenstates, and are shown in Fig. 2.2. The right eigenstates are just the four corner states identified in the Hermitian QI [7], albeit with modified spatial localization lengths:

$$|\psi_1\rangle = \sum_{x,y} \left(-\frac{t-\gamma}{\lambda}\right)^{x+y} |x, y, 1\rangle, \quad (2.3a)$$

$$|\psi_2\rangle = \sum_{x,y} \left(-\frac{t+\gamma}{\lambda}\right)^{-x} \left(-\frac{t-\gamma}{\lambda}\right)^y |x, y, 2\rangle, \quad (2.3b)$$

$$|\psi_3\rangle = \sum_{x,y} \left(-\frac{t-\gamma}{\lambda}\right)^x \left(-\frac{t+\gamma}{\lambda}\right)^{-y} |x, y, 3\rangle, \quad (2.3c)$$

$$|\psi_4\rangle = \sum_{x,y} \left(-\frac{t+\gamma}{\lambda}\right)^{-x-y} |x, y, 4\rangle. \quad (2.3d)$$

We verify $H\psi_i \approx 0$ in the thermodynamic limit $N \rightarrow \infty$ in the Supplemental Material. Just as in the Hermitian QI, each corner hosts one corner state, which has support on only one sublattice. The corresponding left and right eigenstates occupy the same corner. We refer to this parameter regime as “near-Hermitian”. All four (right) eigenstates can be resonantly excited using an external source in a way similar to the Hermitian case (see the Supplemental Material). Ref. [59] was only able to identify one of the four approximate eigenstates using eigendecomposition.

The situation is very different as we enter the *intermediate* regime $\sqrt{|t^2 - \gamma^2|} <$

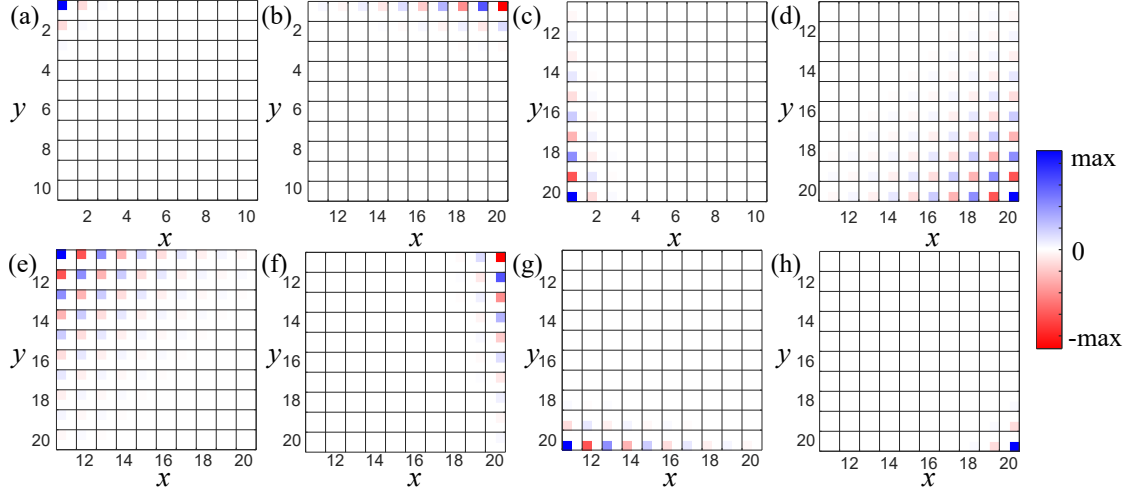


Figure 2.2: Field distribution of (a-d) four zero-energy right eigenstates and (e-h) corresponding left eigenstates of the non-Hermitian QI with open boundary condition in the “near-Hermitian” regime $t = 0.6, \gamma = 0.4, \lambda = 1.5$. Domain size: 20×20 unit cells.

$|\lambda| < |t| + |\gamma|$ (Fig. 2.1(b) cyan). The system still has zero as an eigenvalue of algebraic multiplicity four, but the Schur form of this invariant subspace is now

$$J_0 = \begin{pmatrix} 0 & -\kappa & 0 & 0 \\ 0 & 0 & 0 & 0 \\ 0 & 0 & 0 & \kappa \\ 0 & 0 & 0 & 0 \end{pmatrix}, \quad (2.4)$$

where κ is a function of parameters. For example, $\kappa \approx 0.8246$ when $t = 0.6, \gamma = 0.4, \lambda = 0.7$. The left and right basis states are shown in Fig. 2.3. From the form of J_0 , we know that in this regime the zero energy block is *defective*, and only the first (Fig. 2.3(a)) and third (Fig. 2.3(c)) right basis states are (right) eigenstates; the other two are sometimes called generalized eigenstates. Fig. 2.3(a) is similar to Fig. 2.2(a), but Fig. 2.3(c) is new, and has support on two (2 and 3) sublattices¹.

We refer to the former as “mono-sublattice”, and the latter “multi-sublattice”.

Another major difference from the near-Hermitian regime is that all four right

¹Similar corner states have been predicted in a Hermitian model in [55], but there the bulk is gapless.

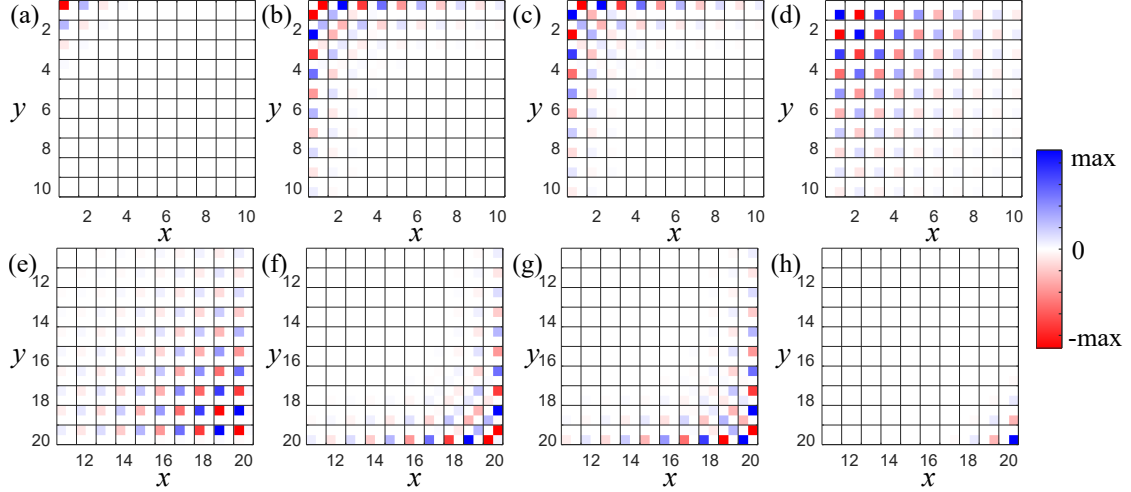


Figure 2.3: Field distribution of (a-d) four zero-energy right basis states and (e-h) corresponding left basis states of the non-Hermitian QI with open boundary condition in the intermediate regime $t = 0.6, \gamma = 0.4, \lambda = 0.7$. Domain size: 20×20 unit cells.

basis states are localized at the top-left corner, while all four left basis states are localized at the bottom-right corner.

We note that this is a perfect example of how a few-level non-Hermitian (or more specifically, defective) model, like Eq. (2.4), can emerge from a large, quasi-continuous system. Many studies in the field of non-Hermitian physics start from a two-level model [13, 33, 18], but our work shows how the collective behavior of lattice sites can serve as an ingredient of these abstract models.

In a perfect lattice like this, an approximate analytical expression of the basis

states can be obtained as

$$\begin{aligned}
|\eta_1^R\rangle &= \sum_{x,y} r_1^{x+y} |x, y, 1\rangle, \\
|\eta_2^R\rangle &= \sum_{x,y} (r_1^x - r_2^x) r_1^y (|x, y, 2\rangle + |y, x, 3\rangle), \\
|\eta_3^R\rangle &= \sum_{x,y} (r_1^x - r_2^x) r_1^y (|x, y, 2\rangle - |y, x, 3\rangle), \\
|\eta_4^R\rangle &= \sum_{x,y} (r_1^x - r_2^x)(r_1^y - r_2^y) |x, y, 4\rangle, \\
\langle \eta_1^L | &= A_1 \sum_{x,y} (r_1^{\bar{x}} - r_2^{\bar{x}})(r_1^{\bar{y}} - r_2^{\bar{y}}) \langle x, y, 1|, \\
\langle \eta_2^L | &= A_2 \sum_{x,y} r_1^{\bar{x}}(r_1^{\bar{y}} - r_2^{\bar{y}}) (\langle x, y, 2| + \langle y, x, 3|), \\
\langle \eta_3^L | &= A_3 \sum_{x,y} r_1^{\bar{x}}(r_1^{\bar{y}} - r_2^{\bar{y}}) (\langle x, y, 2| - \langle y, x, 3|), \\
\langle \eta_4^L | &= A_4 \sum_{x,y} r_1^{\bar{x}+\bar{y}} \langle x, y, 4|,
\end{aligned} \tag{2.5}$$

where $r_1 = -(t - \gamma)/\lambda$, $r_2 = -\lambda/(t + \gamma)$, $\bar{x} = N + 1 - x$, $\bar{y} = N + 1 - y$. It can be directly verified that $\langle \eta_m^L | \eta_n^R \rangle = 0$ for $m \neq n$ as required. Normalization constants $A_n \sim r_2^{-2N}$ so that $\langle \eta_n^L | \eta_n^R \rangle = 1$. The normalization constants are huge simply because left and right states are localized at opposite corners. Under this choice

$$J_0 = \begin{pmatrix} 0 & 2\kappa & 0 & 0 \\ 0 & 0 & 0 & 0 \\ 0 & 0 & 0 & \kappa \\ 0 & 0 & 0 & 0 \end{pmatrix}, \tag{2.6}$$

where $\kappa = t + \gamma - \lambda^2/(t - \gamma)$. J_0 and the value of κ are slightly different from those obtained from numerical Schur decomposition, purely due to normalization. In a more complicated lattice or a lattice with random variation (e.g., due to limit of fabrication accuracy), it may be impossible to obtain an analytical solution, but we can still rely on the numerical Schur decomposition.

When the inter-cell hopping amplitude is further reduced to $|\lambda| < \sqrt{|t^2 - \gamma^2|}$, zero-energy corner states disappear (trivial regime). The three regimes of a square finite-sized non-Hermitian QI with open boundary conditions are summarized by a phase diagram shown in Fig. 2.1(b).

The resonant excitation of our non-Hermitian QI in the intermediate regime is drastically different from that of Hermitian QI. First, we present the results of driven simulations with localized sources, and then interpret the results using the Jordan decomposition that we just obtained. The responses of the system introduced in Fig. 2.3 (see the caption for the lattice parameters) to external sources (with zero frequency) localized at different sub-lattice sites are shown in Fig. 2.4(a-c). Surprisingly, our simulations reveal that the response is “non-local”: placing the source at the bottom-right corner gives the strongest excitation of the top-left corner states, whereas in Hermitian systems, one always finds it most efficient to place the source in close proximity of the targeted state’s maximum. Moreover, we find that the response is very sensitive to which sublattice the source is on: the mono-sublattice state is predominantly excited by placing the source on the sublattices 1, 2, or 3. On the other hand, the multi-sublattice state is predominantly excited when the source is on the sublattice 4. Finally, the response in the intermediate regime is much larger compared to that in the near-Hermitian regime (compare Fig. S3 and Fig. 2.4).

If we did not have the knowledge of Jordan decomposition of our system, these excitation behaviors would indeed seem very exotic and hard to explain.

As mentioned earlier, the driven equation $(E - H + i\Gamma)\psi = \xi$ reduces to $(E - J + i\Gamma)\psi' = \xi'$ where $\xi' = P^{-1}\xi$, $\psi = P\psi'$. To understand the behavior of H near $E = 0$, we only need to work in the above mentioned four-dimensional subspace because

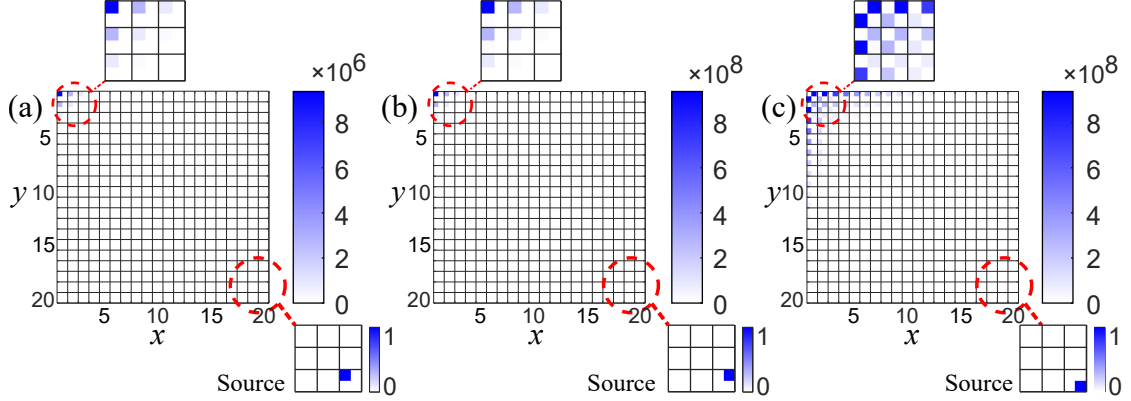


Figure 2.4: The response of a non-Hermitian QI in the intermediate regime to external sources placed at different sub-lattice sites in the lower-right corner of the domain. The source sublattice sites are 1 (left), 2 (middle), and 4 (right). Color: magnitude of the complex field ψ . Mono-sublattice (left and middle) and multi-sublattice (right) corner states are predominantly excited (cf. Fig. 2.3). Source frequency: $E = 0$, small uniform on-site loss $\Gamma = 0.01$. Other lattice parameters (domain size and hopping amplitudes) of the tight-binding model: same as in Fig. 2.3.

only the vectors in this subspace can diverge as $1/E$ or faster. Therefore, below we appropriate the notations ξ' and ψ' to just represent the four dimensional vectors. As mentioned, the resolvent $(E - J_0 + i\Gamma)^{-1}$ is easy to compute (using Eq. (2.6)):

$$(E - J_0)^{-1} = \begin{pmatrix} 1/E & 2\kappa/E^2 & 0 & 0 \\ 0 & 1/E & 0 & 0 \\ 0 & 0 & 1/E & \kappa/E^2 \\ 0 & 0 & 0 & 1/E \end{pmatrix}, \quad (2.7)$$

with substitution $E \rightarrow E + i\Gamma$. To calculate ξ' we need to calculate the inner products $\langle \eta_n^L | \xi' \rangle$. From the form of η_n^L we immediately see that placing a source on sublattice 1 gives $\xi' \propto (1, 0, 0, 0)^T$. By calculating $\psi' = (E - J_0 + i\Gamma)^{-1}\xi'$ we know that the mono-sublattice state is excited. Likewise, placing a source on sublattice 4 induces $\xi' \propto (0, 0, 0, 1)^T$, so the multi-sublattice state is excited. Note that placing a source on either sublattice 2 or 3 induces $\xi' \propto (0, 1, \pm 1, 0)^T$, but the mono-sublattice state still dominates due to its faster divergence rate $1/E^2$. This is clearly observed

in Fig. 2.4, where the response to the sources placed on sublattices 2 and 4 (middle and right figures) is stronger than that to the source placed on sublattice 1 (left figure). Placing the source as far away as possible from the corner states leads to stronger excitation of the latter because this maximizes the inner product with η_n^L . The huge amplitude of the response ψ is mainly due to the exponentially large normalization constants A_n .

2.4 Conclusions

We demonstrated the issues of using eigendecomposition in non-Hermitian lattice systems and proposed using Jordan decomposition as a replacement. Jordan decomposition is a reasonable choice since it is a generalization of eigendecomposition and because of its close connection to the equation of motion of the system. We provide procedures of how it can be achieved numerically in a system with spectrally isolated modes. We used a non-Hermitian quadrupole insulator with asymmetric intracell coupling strengths as an example to show how a few-level defective Hamiltonian can emerge from a large lattice and that the delicate and exotic response of the system to external drives can be beautifully explained by the Jordan basis states and the Jordan form.

2.5 Supplemental Material

2.5.1 Spectrum of an open-boundary non-Hermitian quadrupole insulator (QI)

First we briefly show the derivation of the bulk spectrum of an open-boundary non-Hermitian QI, and following it, the gap-closing condition and when the bulk spectrum is real.

The Bloch Hamiltonian of the non-Hermitian QI corresponding to Fig. 1(a) is

$$H(k_x, k_y) = [t + \lambda \cos k_y] \tau_x + [\lambda \sin k_y + i\gamma] \tau_y + [t + \lambda \cos k_x] \tau_z \sigma_x + [\lambda \sin k_x + i\gamma] \tau_z \sigma_y, \quad (2.8)$$

where we have set the lattice constant $a_0 = 1$, and τ_i and σ_i ($i = x, y, z$) are Pauli matrices for degrees of freedom within a unit cell.

As mentioned in the paper, to correctly calculate the bulk spectrum of a non-Hermitian QI under open boundary condition, one has to make the following substitution in the Bloch Hamiltonian: $(k_x, k_y) \rightarrow (k_x - i \ln \beta_0, k_y - i \ln \beta_0)$, where $\beta_0 = \sqrt{|(t - \gamma)/(t + \gamma)|}$.

The eigenvalues E of the resulting Hamiltonian are doubly degenerate and

$$E^2(k_x, k_y) = 2(t^2 - \gamma^2 + \lambda^2) + \lambda \sqrt{|t^2 - \gamma^2|} [\text{sgn}(t + \gamma)(e^{ik_x} + e^{ik_y}) + \text{sgn}(t - \gamma)(e^{-ik_x} + e^{-ik_y})]. \quad (2.9)$$

It is straightforward to see that the bulk spectrum is real when $|t| > |\gamma|$. $E = 0$ (for some real (k_x, k_y)) gives the gap-closing condition $t^2 = \gamma^2 \pm \lambda^2$.

The complete spectrum of the open-boundary non-Hermitian QI in the “near-Hermitian” regime, with parameters the same as in Fig. 2 is shown in Fig. 2.5(a).

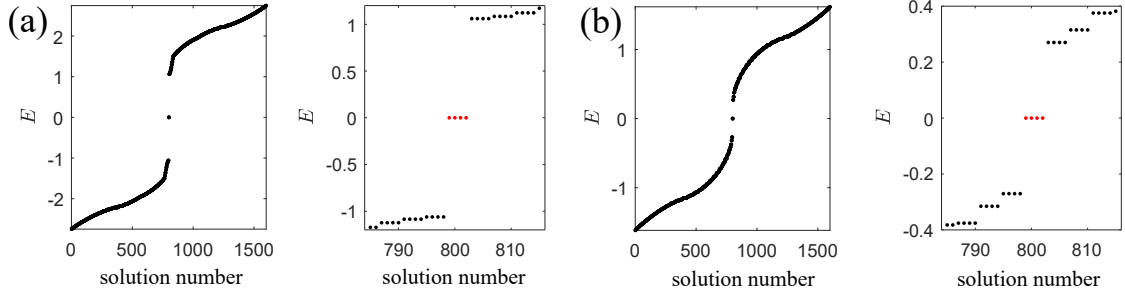


Figure 2.5: Spectra of open-boundary non-Hermitian QIs. (a) Near-Hermitian regime. Left: full spectrum. Right: a zoom-in at the zero-energy corner states (red). Parameters: same as in Fig. 2 ($t = 0.6, \gamma = 0.4, \lambda = 1.5, N = 20$). (b) Intermediate regime. Left: full spectrum. Right: a zoom-in at the zero-energy corner states (red). Parameters: same as in Fig. 3 ($t = 0.6, \gamma = 0.4, \lambda = 0.7, N = 20$).

The bulk bandgap as predicted in the previous section, as well as four eigenvalues of $E = 0$ (see the zoom-in at right) are clearly visible.

The complete spectrum of the open-boundary non-Hermitian QI in the “intermediate” regime, with parameters the same as in Fig. 3 is shown in Fig. 2.5(b). The bulk bandgap is smaller but still clear, and four eigenvalues of $E = 0$ are present. Note that this only means the algebraic multiplicity of the $E = 0$ eigenvalue is 4. As demonstrated in the paper, there are only 2 linearly independent corner states, i.e., the geometric multiplicity of the $E = 0$ eigenvalue is 2.

As mentioned in the paper, both parameter sets fall in to the region where the system has a purely real spectrum.

2.5.2 Analytic verification of corner states

In this section we verify that the corner states with field distribution given in the paper are indeed approximate eigenstates of the Hamiltonian.

In the near Hermitian regime, there are 4 corner states, with field distribution

in the same fashion, see Eq. (3). Similar analytical solutions have been obtained for localized states in Hermitian systems [3, 69, 55]. Here we just demonstrate $H|\psi_1\rangle \approx 0$. Apparently $\langle x, y, 1|H|\psi_1\rangle = \langle x, y, 4|H|\psi_1\rangle = 0$ for all x, y .

$$\langle x, y, 2|H|\psi_1\rangle = (t - \gamma)(-\frac{t - \gamma}{\lambda})^{x+y} + \lambda(-\frac{t - \gamma}{\lambda})^{x+1+y} = 0, \quad (2.10)$$

$$\langle x, y, 3|H|\psi_1\rangle = (t - \gamma)(-\frac{t - \gamma}{\lambda})^{x+y} + \lambda(-\frac{t - \gamma}{\lambda})^{x+y+1} = 0. \quad (2.11)$$

The only exception to the above two equations happens at edges $x = N$ and $y = N$. But in the thermodynamic limit $N \rightarrow \infty$ the field is exponentially weak at those edges. Thus ψ_1 is an approximate eigenstate of the Hamiltonian, and so is ψ_2, ψ_3, ψ_4 .

In the intermediate regime, ψ_1 survives as the superlocalized state, so we only need to verify that the sublocalized state η_3^R in Eq. (5) is an approximate eigenstate. Again it is apparent that $\langle x, y, 2|H|\eta_3^R\rangle = \langle x, y, 3|H|\eta_3^R\rangle = 0$ for all x, y .

$$\begin{aligned} \langle x, y, 1|H|\eta_3^R\rangle &= (t + \gamma)(r_1^x - r_2^x)r_1^y + \lambda(r_1^{x-1} - r_2^{x-1})r_1^y - (t + \gamma)(r_1^y - r_2^y)r_1^x - \lambda(r_1^{y-1} - r_2^{y-1})r_1^x \\ &= (t + \gamma)r_1^{x+y} + \lambda r_1^{x-1+y} - (t + \gamma)r_1^{y+x} - \lambda r_1^{y-1+x} = 0, \end{aligned} \quad (2.12)$$

$$\begin{aligned} \langle x, y, 4|H|\eta_3^R\rangle &= (t - \gamma)(r_1^x - r_2^x)r_1^y + \lambda(r_1^x - r_2^x)r_1^{y+1} + (t - \gamma)(r_1^y - r_2^y)r_1^x + \lambda(r_1^y - r_2^y)r_1^{x+1} \\ &= 0 + 0 = 0. \end{aligned} \quad (2.13)$$

Note that the form of the solution satisfies $\eta_3^R(0, y, 2) = \eta_3^R(x, 0, 3) = 0$ which is compatible with the open boundary condition, so the above calculation is also valid for boundary sites $x = 1$ and $y = 1$. Again the only exception happens at edges $x = N$ and $y = N$, but since the field is exponentially weak there, η_3^R is an approximate eigenstate of the Hamiltonian.

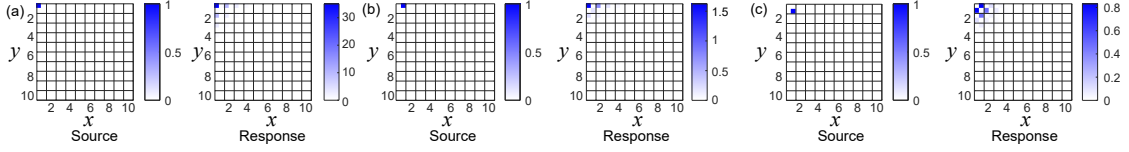


Figure 2.6: The response of a non-Hermitian QI in the intermediate regime to sources placed at different sub-lattice sites in the top-left corner of the domain. The source sublattice sites are 1 (left), 2 (middle), and 4 (right). Color in response plots: magnitude of the complex field ψ . Source frequency: $E = 0$, uniform on-site loss: $\Gamma = 0.01$. Other lattice parameters (domain size and hopping amplitudes) of the tight-binding model: same as in Fig. 3.

2.5.3 Additional examples of excitation of corner states in the intermediate regime

As mentioned in the main text, in the intermediate regime a source at the top-left corner will only lead to much weaker response compared to a source at the bottom right corner. We show the data here in Fig. 2.6.

2.5.4 Excitation of corner states in the near-Hermitian regime

As mentioned in the main text, in the near-Hermitian regime the response of the system near zero energy is similar to that of a Hermitian QI. For completeness we show the numerical results here. Fig. 2.7(a-c) shows that, placing the source at a corner excites the corner state that is localized at that corner. This is because in this regime, the left and right eigenvectors of a corner state are localized at the same corner. In Fig. 2.7(d) we put sources of equal amplitude on the four sublattices of the bottom-right unit cell, but the response is almost identical to Fig. 2.7(c), showing that unlike in the intermediate regime, here it is practically

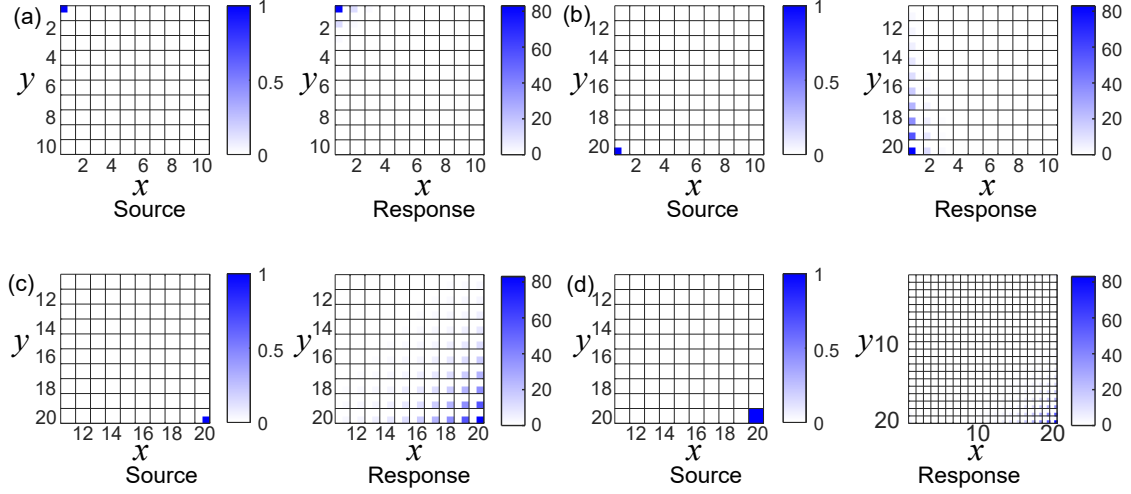


Figure 2.7: The response of a non-Hermitian QI in near-Hermitian regime to external source at different corners. Color: magnitude of the complex field ψ . (a) Source is placed on $|x, y, j\rangle = |1, 1, 1\rangle$. (b) Source is placed on $|1, 20, 3\rangle$. (c) Source is placed on $|20, 20, 4\rangle$. (d) Sources of equal amplitude are placed on the four sublattices of the bottom-right unit cell, i.e., $|20, 20, j\rangle, j = 1, 2, 3, 4$. Source frequency $E = 0$, uniform on-site loss $\Gamma = 0.01$. Other parameters: same as in Fig. 2 ($t = 0.6, \gamma = 0.4, \lambda = 1.5, N = 20$).

impossible to excite an corner state that locates far away from the source.

CHAPTER 3

**BAND REPULSION IN CONDENSED MATTER AND
ELECTROMAGNETIC SYSTEMS**

3.1 Introduction and Motivation

The relationship between particle's energy $\varepsilon(\mathbf{p})$ and momentum \mathbf{p} (or, in the context of wave excitation that have no particle equivalent, between the frequency $\omega(\mathbf{k})$ and the wavenumber \mathbf{k}) is one of its most fundamental properties. Both quantities are conserved for time-independent spatially-uniform media as the consequence of the continuous time-shifting and translational symmetries. In the simplest one-dimensional case of $\mathbf{p} = p\mathbf{e}_x$, the relationship between $\varepsilon(p)$ and p is often referred to as the dispersion relationship: a continuous curve with a finite number of interruptions that occur primarily due to the existence of material resonances. For example, polaritons – electromagnetic waves that are part-electromagnetic and part-material excitations – exhibit propagation stop-bands corresponding to frequency ranges inside which no propagating polaritons exist, i.e. the equation $\omega(k) = \omega_0$ has no real-valued solutions for any value of ω_0 inside the stop-band.

The situation changes dramatically when the medium is modulated in space or time. In the former case, a periodically-modulated medium is referred to as a photonic crystal (PhC) [93, 40]. The existence of propagation bandgaps in frequency invoked the comparison of the PhCs to “semiconductors of light”. While the continuous translational symmetry in PhCs is broken, a new discrete symmetry – translation by an integer number of spatial periods of the length a – gives rise to the conservation of a quasi-momentum (also referred to as a Bloch wavenumber) \bar{k} bounded by the edges of the Brillouin zone: $-\pi/a < \bar{k} < \pi/a$. The resulting dis-

persion curves $\omega(\bar{k})$ have a relatively simple topology: a set of propagation bands stretching across the entire Brillouin zone (i.e., no gaps in \bar{k}), with different bands separated from each other by frequency stop-bands. Other systems, such as periodically time-modulated systems, known as photonic time crystals (PTCs), have been introduced by analogy [36, 80, 11, 106, 105]. The discrete time-shift symmetry by an integer number of periods T gives rise to quasi-frequencies $\bar{\omega}(k)$ that also form propagation bands. The topology of time-crystal (TC) bands is distinct from that of the PhCs: the gaps are formed in k while the quasi-frequencies span the entire Floquet zone: $-\pi/T < \bar{\omega} < \pi/T$ [63].

In general, a physical system can possess spatial periodicities *and* be simultaneously modulated in time. A Floquet crystal (FCs) exemplifies a two-dimensional version of such a system. The band structures of the FCs consist of the propagation bands separated by gaps in quasi-energy $\bar{\varepsilon}$ and no gaps in the quasi-momentum \bar{p} , i.e. they are equivalent to those of the PhCs. Because of the two-dimensional nature of the FCs, and the accessibility of the entire Brillouin zone to propagating (bulk) states, their propagation bands can possess nontrivial topology in the momentum space. Such topology is exemplified by the so-called “Floquet topological insulators” (FTI) [45, 58, 46], as well as their photonic [74, 34] and phononic [22] analogues.

It is natural to ask why the geometry of the propagation bands is so starkly different between the PhCs/FCs (bandgaps in quasi-frequency or energy, respectively) and the PTCs (bandgaps in wavenumber). The distinction between FCs and PTCs is particularly puzzling because both are induced by time-periodic modulations. In this paper, we systematically answer this question by showing that these two types of driven systems can be transformed into each other, and that it

is possible to obtain gaps in both quasi-energy and quasi-momentum for at least some periodically-modulated systems. In what follows, we will be using frequencies/wavenumbers regardless of the model because wave-particle dualism implies a proportionality coefficient (the Planck's constant \hbar , which we set to unity for convenience) between (ε, p) and (ω, k) .

The rest of the manuscript is organized as follows. In Section 3.2, we use a two-level long wavelength model to discuss the criteria for the existence of time- or Floquet-crystals. We present examples for both types of bandgaps, in quasi-frequency ω or wavenumber k corresponding to FCs and TCs, respectively. We further discuss the emergence of simultaneous bandgaps in ω and k that result in closed-curve band diagrams. Our numerical calculations are backed up by the perturbation theory near band crossings. These analytic calculations are used to predict the band topology. In Section 3.4, we turn our attention to electromagnetic systems, and show that similar band diagrams can be obtained, although the criteria for the existence of TCs or FCs are somewhat different. An important observation is that electromagnetism posses time-space duality, whose consequences are also discussed. Finally we address the differences of gaps in frequency or wavevector, as well as those of “interfaces” in space or time, on two sides of which the parameters of the system are different.

3.2 Time- and Floquet-crystals: Examples and Existence Criteria

As an example, we consider a time-periodic system described by a Dirac-type equation in the reciprocal (\mathbf{k} -) space:

$$i\frac{\partial\psi_{\mathbf{k}}(t)}{\partial t} = H(\mathbf{k}, t)\psi_{\mathbf{k}}(t), \quad (3.1)$$

where the system's Hamiltonian is described by a 2×2 matrix $H(\mathbf{k}, t)$ acting on a two-component spinor $\psi_{\mathbf{k}}(t)$. The wave function is assumed to be a spinor (i.e. to have 2 components) describing quantum systems such as graphene or the Su-Schrieffer-Heeger (SSH) model of polyethylene [70, 83], as well as photonic systems possessing both electric and magnetic fields [39]. This model can be generalized to larger numbers of degrees of freedom (DOFs) to account for orbit, spin, valley, and other discrete DOFs. We further assume that $H(\mathbf{k}, t) = H(\mathbf{k}, t + T)$. For a general spatially-periodic system, $H(\mathbf{k}, t)$ is the instantaneous reciprocal space Hamiltonian that can be derived from, for example, a $\mathbf{k} \cdot \mathbf{p}$ theory or a tight-binding model.

The Bloch-Floquet theory states that the solutions of Eq.(3.1) have the form of $\psi_{\mathbf{k}}(t) = e^{-i\omega(\mathbf{k})t}u_{\mathbf{k}}(t)$, where $u_{\mathbf{k}}(t)$ has the periodicity T , and $\omega(k)$ is the quasi-energy to be found by solving the following eigenvalue equation:

$$\left[-i\frac{d}{dt} + H(\mathbf{k}, t) \right] u_{\mathbf{k}}(t) = \omega(\mathbf{k})u_{\mathbf{k}}(t). \quad (3.2)$$

Assuming that the instantaneous Hamiltonian $H(\mathbf{k}, t)$ is self-adjoint (i.e. represented by an Hermitian matrix) and noting that the operator $i\frac{d}{dt}$ is also self-adjoint under the periodic boundary condition, we conclude that all quasi-frequencies $\omega^{(n)}(\mathbf{k})$ (where n is a band number) must be real-valued for every real quasi-

momentum k . Therefore, propagation bandgaps can exist in quasi-frequency, i.e. between the maxima/minima of the $\omega^{(n)}(\mathbf{k})/\omega^{(n+1)}(\mathbf{k})$ bands.

On the contrary, bandgaps in the Bloch wavenumber \mathbf{k} are ruled out because their existence would imply the existence of complex-valued ω -eigenvalues of Eq.(3.2). This would be the case, for example, for FCs (including FTIs) that can be described using a self-adjoint Hamiltonian matrix [74, 34, 22]. Note that the non-Hermitian nature of the Hamiltonian does not imply explicit losses or gain (e.g., the presence of lossy or active materials in the context of photonics). As explained below, it merely implies that the matrix representing the Hamiltonian in any complete basis is not self-adjoint. Therefore, we conclude that the necessary condition for creating bandgaps in Bloch wavenumber is that the instantaneous Hamiltonian $H_{\mathbf{k}}(t)$ is not Hermitian at all times.

3.2.1 A linearized Hamiltonian and the bandgap existence criteria

While the self-adjoint property of a general Hamiltonian $H(\mathbf{k}, t)$ can be used to rule out bandgaps in \mathbf{k} , further assumptions need to be made to describe the opposite situation: bandgaps in \mathbf{k} but not in ω . For that, we assume an isotropic medium and assume a “toy” Hamiltonian $\tilde{H}(k, t)$ linearized in $k = |\mathbf{k}|$. This happens, for example, in the long-wavelength limit, as well as when one expands a Hamiltonian around some k_0 . Equation (3.2) corresponding to $H(\mathbf{k}, t) \equiv \tilde{H}(k, t)$ can then be recast as an eigenvalue problem with respect to k . Specifically, we choose

$$\tilde{H}(k, t) = k\sigma_i + \kappa A(t) \quad (3.3)$$

where σ_i is one of the Pauli matrices ($i = x, y, z$), $A(t)$ is a two-by-two normalized time-periodic modulation matrix, and a real-valued κ is its amplitude. In the absence of the time-dependent modulation, the dispersion relation for the modes governed by the unperturbed Hamiltonian $\tilde{H}_0(k) = k\sigma_i$ is given by $\omega_0^2(k) = k^2$ regardless of i . Therefore, the unperturbed Hamiltonian describes free massless particles or waves in a homogeneous medium, and we can choose $\sigma_i = \sigma_y$ without lack of generality.

With a finite time-periodic perturbation with period T , the eigenvalue problem corresponding to \tilde{H} can be recast with respect to the eigenvalue k :

$$\left[i\sigma_i \frac{d}{dt} + \omega\sigma_i - \sigma_i\kappa A(t) \right] u(k, t) = ku(k, t). \quad (3.4)$$

Likewise, Eq.(3.2) can be expressed with respect to the eigenvalue ω :

$$\left[-i\frac{d}{dt} + k\sigma_i + \kappa A(t) \right] u(k, t) = \omega u(k, t). \quad (3.5)$$

Therefore, noting that $i\sigma_i d/dt$ is a self-adjoint operator, we conclude from Eq.(3.4) that it is sufficient for $\sigma_i A(t)$ to be Hermitian in order for k to be real-valued. Therefore, no bandgaps in ω are allowed in this case because that would imply the existence of a complex-valued k for all values of ω inside such a bandgap. At the same time, if $\sigma_i A(t)$ is a self-adjoint but $A(t)$ is not, then it follows from Eq.(3.5) that a finite gap in k is allowed because ω is not necessarily real-valued. Similarly, only the bandgaps in ω are permitted if $A(t)$ is a self-adjoint matrix, but $\sigma_i A(t)$ is not. Note that such situations are possible because, in general, σ_i and $A(t)$ are non-commuting: $\sigma_i A \neq A\sigma_i$.

3.2.2 The linearized Hamiltonian: examples

Below we consider several examples of time-modulated “toy” Hamiltonians $\tilde{H}(k, t)$ with $\sigma_i = \sigma_y$, and use these examples to illustrate band gap openings in quasi-frequency ω ($A \equiv A_1(t)$: FCs), in Bloch wavenumber k ($A \equiv A_2(t)$: TCs), or simultaneously in ω and k . The latter case has not been considered before, and we refer to such systems as Floquet Time Crystals (FTCs).

Assuming that the period of the perturbation is $T = \pi$, we find that the band structure in the limit of vanishing amplitude of $A(t)$ consists of four straight dispersion lines forming a square that are obtained by displacing the $\omega = \pm k$ linear dispersion curves by $\Omega \equiv 2\pi/T = 2$. Therefore, the unmodulated ($\kappa = 0$) band structure has no gaps in either k or ω . These bands are shown in Fig. 3.1(a). However, a finite-amplitude time-dependent modulation distorts the propagation bands and opens the bandgaps as described below. In both Refs. [34, 22] the modulation is on diagonal elements of the Hamiltonian; in this paper we mainly demonstrate examples with modulation on off-diagonal elements.

As an example of an FC, we consider $A_1 = \frac{1}{2} \begin{pmatrix} 0 & \exp(2\pi i t/T) \\ \exp(-2\pi i t/T) & 0 \end{pmatrix}$. While

A_1 is Hermitian (no gaps in k), $\sigma_y A_1$ is not because $\sigma_y A_1 \neq A_1 \sigma_y$. Therefore, it is natural that the perturbed bands appear as in Fig. 3.1(a). The gap in quasi-frequency ω observed in Fig. 3.1(a) is characteristic of FCs and time-independent PhCs. The propagation bands $\omega(k)$ plotted in Fig. 3.1(b) are calculated by solving an eigenvalue Eq. (3.5) for each value of k , subject to the periodicity condition $u(k, t = 0) = u(k, t = T)$. This example shows that frequency bandgaps can emerge even in the absence of explicit spatial periodicity, as would be the case with time-independent PhCs.

The next example corresponds to $A_2 = \frac{1}{2} \begin{pmatrix} 0 & i \sin(2\pi t/T) \\ i \cos(2\pi t/T) & 0 \end{pmatrix}$. Now, on the contrary, $\sigma_y A_2$ is Hermitian (no gaps in ω) while A_2 is not (possible gaps in k). The perturbed bands shown in Fig. 3.1(c) indeed reveal a gap in the Bloch momentum k , which is characteristic of TCs. This kind of gaps comes with pairs of exceptional points, for example here one at $k \approx \pm 0.06$, and another at $k \approx 1.99$ and $k \approx 2.05$ (the last one not shown in the figure). The propagation bands $k(\omega)$ plotted in Fig. 3.1(b) are calculated by solving an eigenvalue differential equation (3.4) for each value of ω , subject to $u(k, t=0) = u(k, t=T)$.

A qualitative explanation of the gap around $k_0 = \pm 1$ is as follows. In the absence of time-periodic drive, the natural frequency of the modes with $k = \pm k_0$ is $\omega_0 = 1$. On the other hand, the time-periodic drive corresponds to the frequency of $\Omega = 2\pi/T = 2$, i.e. $\Omega = 2\omega_0$. When one of the parameters of an oscillating system varies with twice the system's natural frequency, parametric instability ensues [51]. Because the frequency of an unstable parametrically driven system is complex (i.e. there are two solutions: an exponentially growing and an exponentially decaying ones), a gap is formed around k_0 . The size of the gap depends on the strength of the parametric drive because multiple wavenumbers $k \approx k_0$ with corresponding frequencies $\omega_0(k) \approx 1$ around the central wavenumber k_0 can be driven parametrically-unstable by a finite-amplitude drive.

Finally, we consider the third case: $A_3 = \frac{1}{2} \begin{pmatrix} 0 & \sin(2\pi t/T) \\ \cos(2\pi t/T) & 0 \end{pmatrix}$. Here, neither A_3 nor $\sigma_y A_3$ are Hermitian. Bandgaps in both k and ω are allowed in this case. In principle, the dispersion bands can form closed curves, as indeed shown in Fig. 3.1(d). Note that the violation of both Hermiticity requirements does not guarantee bandgaps, as in some fine-tuned cases there can be no gap

at all. One such case is when $A_{\text{imp}}(t) = -ik \sin(2\pi t/T) \sigma_y$. While neither $A(t)$ nor $\sigma_y A(t)$ is Hermitian, one can verify that $u(t) = (1, \pm i)^T e^{\kappa \cos(2\pi t/T)}$ are eigenfunctions with eigenvalues $\omega = \pm k$. It can be shown that the gap vanishes whenever $A_{\text{imp}}(t)$ and σ_y commute. As we show below, such perturbation can be interpreted as impedance-preserving in the context of photonics.

We further note that for all three perturbation matrices A_j (where $j = 1\dots 3$) real-valued dispersion curves $\omega(k)$ are present. This is because we have simply chosen harmonics for all the entries. Naively averaging the perturbation matrices over a period would give zero. This is similar to PT-symmetry systems, where gain and loss at different parts of the system is balanced [18]. In these systems, the spectra can be purely real in part of, but not the entire parameter space. Similarly, in our systems here, the non-Hermiticity introduced at different t averages out to zero, and therefore for most values of k , ω is real. Another way to see why this happens is, as we will show in the next section, at least up to the first or second order perturbation, the dispersion near a band crossing point always has the form of a hyperbola: $(\omega - \omega_0)^2 - (k - k_0)^2 = \text{const}$, where the real constant can be either positive or negative, giving rise to real-valued dispersion curves. In the next Section, we develop an analytic theory that explicitly demonstrates the existence and size of the bandgaps in ω and k , as well as their scaling with κ . This is accomplished by developing a time-averaging perturbation theory that yields a time-averaged k -dependent Hamiltonian $\mathcal{H}(k) \equiv \langle \tilde{H}(k, t) \rangle$.

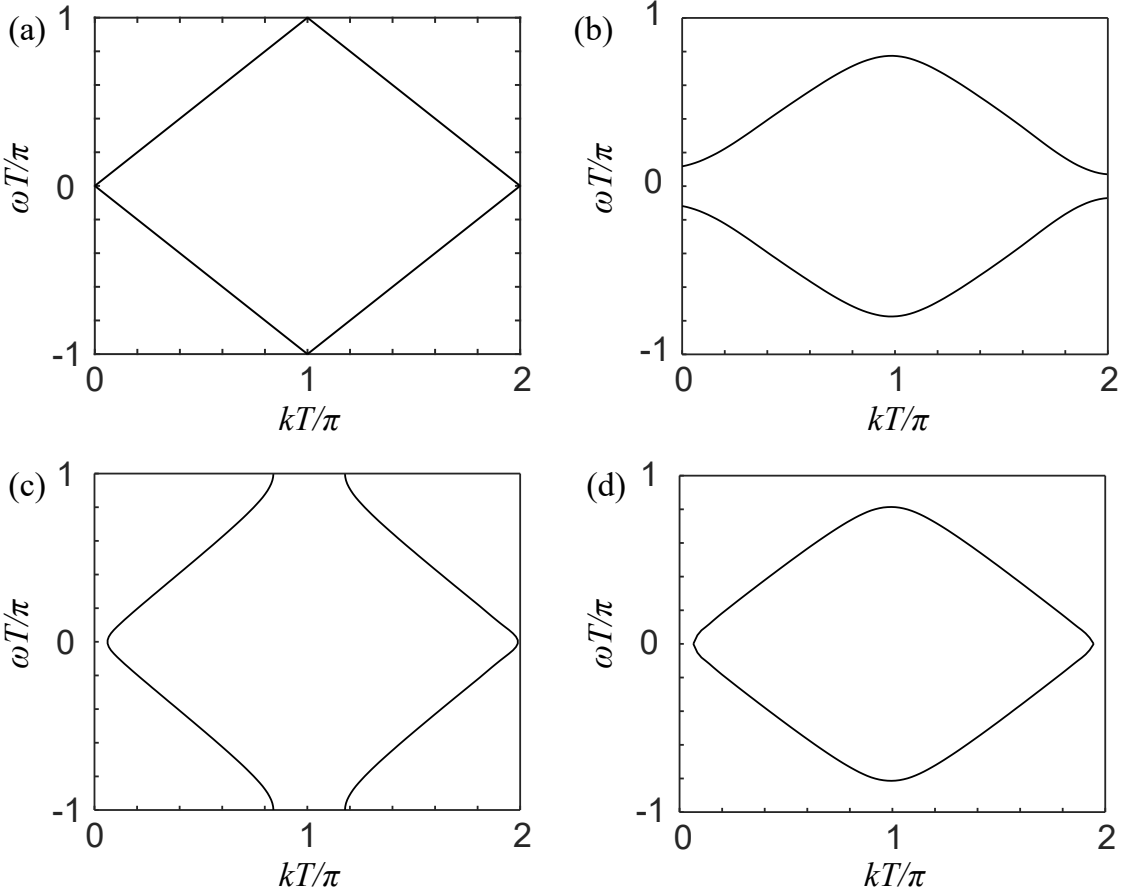


Figure 3.1: Classification of the dispersion curves corresponding to an unperturbed Hamiltonian $\tilde{H}_0(k) = k\sigma_y$ subjected to time-periodic perturbations: $\tilde{H}(k, t) = \tilde{H}_0(k) + \kappa \mathbf{A}(\mathbf{t})$. To illustrate various types of bandgap openings, the perturbation matrices are chosen as (a) $\kappa = 0$ (unperturbed bands), (b) $A = A_1$ (bandgap opening in ω : FC), (c) $A = A_2$ (bandgap opening in k : TC), and (d) $A = A_3$ (bandgap openings in ω and k : FTC). Only the modes with simultaneously real-valued ω and k are plotted. See text for the definitions of $A_{1,2,3}$. The bands are plotted within the first Floquet zone of the quasi-frequencies: $-\pi/T < \omega < \pi/T$. Parameter: $\kappa = \pi/T$.

3.3 Perturbation Theory near Band Crossings

The perturbed time-averaged Hamiltonian $\mathcal{H}(k) \equiv k\sigma_i + \Delta\mathcal{H}(k)$ produced by the time-dependent periodic modulation $A(t)$ can be approximately calculated in the proximity of each of the four band-crossing points shown in Fig. 3.1(a). Here, the band-crossing points $\mathbf{G}_l \equiv (k_l, \omega_l)$ (where $l = 1, \dots, 4$) are as follows: $\mathbf{G}_1 = (0, 0)$,

$\mathbf{G}_{2,3} = (\pi/T, \pm\pi/T)$, and $\mathbf{G}_4 = (2\pi/T, 0)$. The perturbed low-energy (i.e. expanded to the lowest order in $\delta k = k - k_l$) Hamiltonian can inform us about the direction of the bandgap opening (i.e. in k or in ω), as well as predict the topology of the perturbed propagation bands. The time-averaged Hamiltonian also serves as a convenient explanation of the bands shown in Fig. 3.1(b-d).

We start by defining the unperturbed states ($\kappa = 0$) that are shown in Fig. 3.1(a) as artificially band-folded. These eigenstates of σ_i are eigenspinors $|\pm\rangle$ in the i th direction defined by $k\sigma_i|\pm\rangle = \pm k|\pm\rangle$, with their corresponding eigen-frequencies equal to $\omega_{\pm} = \pm k$. First, we consider the crossing of the $|+\rangle$ and $|-\rangle$ unperturbed states (no band folding) at the \mathbf{G}_1 point. A standard first-order degenerate perturbation theory [53] tells us that the low-energy Hamiltonian is characterized by the following matrix (in the unperturbed-state basis $\{|+\rangle, |-\rangle\}$):

$$\begin{pmatrix} \omega_+ & \langle +|A_0|-\rangle \\ \langle -|A_0|+ \rangle & \omega_- \end{pmatrix}, \text{ where}$$

$A_0 = T^{-1} \int_0^T A(t)dt$. However, it is usually the convention that a non-zero $A_{k,0}$ would be absorbed into the unperturbed part of H . In that case we see that the first-order contribution is zero. Thus we must resort to the second-order degenerate perturbation theory, and obtain: $\Delta\mathcal{H}(k) = \Omega^{-1}[H_{-1}, H_{+1}]$ [53], where $[A, B] \equiv AB - BA$ is a commutator between two operators/matrices A and B , $\Omega = 2\pi/T$ is the perturbation frequency, and $H_m(k) = T^{-1} \int_0^T e^{im\Omega t} \tilde{H}(k, t)dt$. For example, $H_0 = k\sigma_i$, and $H_1 = \kappa T^{-1} \int_0^T e^{i\Omega t} A(t)dt$. Therefore, the mathematical form of the perturbation $A(t)$ determines the nature of the band crossing.

For the case of $A_1(t)$ discussed earlier and illustrated in Fig. 3.1(b), we find that $[A_{-1}, A_{+1}] = (1/4)\sigma_z$. Therefore, the gap emerging due to $A_1(t)$ is expected to be in quasi-frequency ω , and the perturbation by the $\kappa A_1(t)$ can be interpreted as an ac Stark shift [53] proportional to κ^2 : $\mathcal{H}^{(1)}(k) = k\sigma_y + (\kappa^2/4\Omega)\sigma_z$. This analytic prediction is confirmed by the band structure plotted in Fig. 3.1(b).

This result is contrasted by the case of $A_2(t)$ illustrated in Fig. 3.1(c). In that case we find that $[H_{k,-1}, H_{k,+1}] = (1/8)i\kappa^2\sigma_z$. Therefore, ω is imaginary for $k < (1/8)\kappa^2/\Omega$, and, therefore, the wavevector gap opens around the \mathbf{G}_1 point. This is consistent with the non-Hermitian nature of the original time-dependent Hamiltonian $\tilde{H}(k, t) = \tilde{H}_0(k) + \kappa A_2(t)$, as well as the time-averaged Hamiltonian $\mathcal{H}^{(2)}(k) = k\sigma_y + i(\kappa^2/4)\sigma_z$. A similar situation at the \mathbf{G}_1 point occurs for the $A_3(t)$ case illustrated in Fig. 3.1(d).

It is instructive to explore the implications of such time-periodic perturbation to the 2D version of the $H_0(k)$ Hamiltonian: the Dirac Hamiltonian $H_0^{2D}(\mathbf{k}) = k_x\sigma_x + k_y\sigma_y$ describing a free massless particle with a 2D momentum $\mathbf{k} \equiv (k_x, k_y)$ near the \mathbf{G}_1 point. We observe that the time-averaged perturbation term $[H_{-1}, H_{+1}] = B\sigma_z$ represents a complex-valued mass term, where $B \propto \kappa^2$ is a complex number determined by the details of the perturbation matrix A_m (where $m = 1 \dots 3$). By analogy with graphene, we conclude that by controlling the sign of the Dirac mass (i.e. the sign of B in the case of $m = 1$) we can control the Chern numbers for the propagation bands split by the time-periodic modulation [46, 19]. The sign of B can be flipped by, for example, using A_1^T (the transpose of A_1) instead of A_1 .

Next, we consider the band-crossing at the $\mathbf{G}_2 = (\pi/T, \pi/T)$ point formed by the band $|+\rangle$ and the folded band $e^{i\Omega t}|-\rangle$ (with unperturbed energy $\omega_- + \Omega$). Therefore, in this case the first-order perturbation theory does contribute to the low-energy perturbed Hamiltonian and

$$\mathcal{H}(k) = \begin{pmatrix} \omega_+ & \langle +|H_{+1}(k)|-\rangle \\ \langle -|H_{-1}(k)|+ \rangle & \omega_- + \Omega \end{pmatrix}. \quad (3.6)$$

After some straightforward calculation, we obtain $\mathcal{H}^{(1)}(k) = (\pi/T)I + (\kappa/2)\sigma_y + \delta k\sigma_z$, $\mathcal{H}^{(2)}(k) = (\pi/T)I + (ik/4)\sigma_x + (ik/4)\sigma_y + \delta k\sigma_z$, $\mathcal{H}^{(3)}(k) = (\pi/T)I + (1\kappa/4)\sigma_x +$

$(1\kappa/4)\sigma_y + \delta k\sigma_z$, $\mathcal{H}^{\text{imp}}(\mathbf{k}) = (\pi/T)\mathbf{I} + \delta k\sigma_z$. Therefore, locally the shapes of dispersion curves in Fig. 1 are all hyperbolas: (b) $\delta\omega^2 - \delta k^2 = (\kappa/2)^2$; (c) $\delta\omega^2 - \delta k^2 = -\kappa^2/8$; (d) $\delta\omega^2 - \delta k^2 = \kappa^2/8$. Only the second equation has a negative term on the right hand side, which is consistent with the fact that only Fig. 1(c) has the gap in k at the \mathbf{G}_2 point.

In a 2D system, if $\langle \pm | H_{k,\pm 1} | \mp \rangle$ has the form $\delta k_x \pm i\delta k_y$ near the crossing point, then a band inversion will lead to nontrivial contribution to the Chern number [45, 34]. One specific example is $H^{2D}(\mathbf{k}) = k_x\sigma_x + k_y\sigma_y + M\sigma_z + A^{2D}(t)$, $A^{2D}(t) = \kappa\sigma_z \cos \Omega t$, where $\Omega > 2M$ [58].

These low-energy Hamiltonians discussed above focus on local Berry curvatures and are useful for predicting edge modes. More generally, an effective Hamiltonian can be defined [45] and be used to calculate band Chern numbers. However, since periodically driven systems do not have a well-defined ground state because their spectra are periodic in quasi-energy, band Chern numbers can only determine gap Chern numbers, which appear in the bulk-boundary correspondence, up to an overall constant. In a static system, the bandgap below the ground state naturally has zero Chern number. However, in a time-dependent system, an edge state can go below zero energy and re-emerge at $\omega = \Omega$. In other words, the effective Hamiltonian of the bulk does not contain all information of the system, which is needed to calculate the gap Chern numbers [97].

3.4 Time-periodic perturbations of photonic crystals

In this Section we discuss the applications of the formalism derived in Section 3.2 to electromagnetic systems. First, we consider a spatially homogeneous material

with permittivity $\epsilon(t)$ and permeability $\mu(t)$, which are both modulated in time with period T . Assume instantaneous response of the medium, such that the following constitutive relations hold: $\mathbf{D}(\mathbf{x}, t) = \epsilon(t)\mathbf{E}(\mathbf{x}, t)$ and $\mathbf{B}(\mathbf{x}, t) = \mu(t)\mathbf{H}(\mathbf{x}, t)$. For a specific linear polarization of electromagnetic waves propagating in the z -direction, we obtain: $\mathbf{D}(\mathbf{x}, t) = D(t)e^{ikz}\mathbf{e}_x$ and $\mathbf{B}(\mathbf{x}, t) = B(t)e^{ikz}\mathbf{e}_y$. Under such planar wave assumption, we can recast the wave equation as a generalized eigenvalue problem with an eigenvalue k^2 :

$$k^2 \frac{D(t)}{\epsilon(t)} = -\frac{1}{c^2} \frac{d}{dt} \left[\mu(t) \frac{dD(t)}{dt} \right] \quad (3.7)$$

It follows from the Bloch-Floquet theory that the solution of Eq.(3.7) has the following form $D(t) = e^{-i\omega t}u(t)$ where $u(t)$ has periodicity T . If both $\epsilon(t)$ and $\mu(t)$ are real and positive (condition I), then both the operator $1/\epsilon(t)$ and $\Theta \equiv -\frac{1}{c^2} \frac{d}{dt} \mu(t) \frac{d}{dt}$ are self-adjoint under Floquet periodicity condition, $1/\epsilon(t)$ is positive definite and Θ is positive semi-definite. Together they ensure $k^2 \geq 0$ for any ω , thus $k \in \mathbb{R}$, which means whenever there is an bandgap in the dispersion relation, it must be in wavevector k .

The photonic FTI in Ref. [34] is not restricted by this rule at the expense of spatial modulation. The authors gave an approximate expression for the Floquet eigenvalues: $\omega \approx \omega_1 \pm V \sqrt{\omega_1 \omega_2}$, where $\omega_{1,2}$ are eigenfrequencies of a static system, and V is a coupling strength. Clearly the Floquet eigenvalues are real only if $\omega_{1,2}$ have the same sign, which is only possible if there already is spatial modulation; whereas without spatial modulation, crossings can only be formed by modes with originally opposite-sign frequencies.

The second-order wave equation given by Eq.(3.7) can also be recast into a

Dirac equation-like form:

$$H(t)\psi(t) = i\frac{d\psi(t)}{dt}, \quad \text{where} \quad H(t) = \begin{pmatrix} 0 & ck/\mu(t) \\ ck/\epsilon(t) & 0 \end{pmatrix}, \quad \psi(t) = \begin{pmatrix} D(t) \\ B(t) \end{pmatrix}. \quad (3.8)$$

Similar to the earlier discussion in Section 3.2, if $H(k, t)$ is Hermitian, then $\omega \in \mathbb{R}$, and the bandgaps must be in quasi-frequency. Note that the Hermiticity condition for $H(k, t)$ requires that $\epsilon(t) = \mu^*(t)$ (condition II): a very challenging condition to meet for optical waves because of the well-known difficulty in modulating magnetic properties of materials at optical frequencies [52].

Conditions I and II are simultaneously fulfilled when $\epsilon(t) = \mu(t) \in \mathbb{R}$, i.e. the impedance matching condition is satisfied as discussed in Sec. 3.2. It then follows that there can be no gap at all in the dispersion relation, as was recently found in Ref. [92]. If condition I but not condition II is satisfied, then the bandgaps in the wavevector are expected as illustrated in Fig. 3.2(b). This is indeed the case in PTCs [63]. A topological invariant known as the Zak phase [103] can then be defined for each band. Zak phase is quantized, provided that additional symmetries (e.g., the time inversion symmetry) exists.

If only the condition II is satisfied then there are likely bandgaps in quasienergy, which is similar to the band structures of FTIs. One such example is shown in Fig. 3.2(a). If neither condition is satisfied, then both types of bandgaps can exist at different band crossings, and an example is given in Fig. 3.2(c). In this case the dispersion curve can be a closed curve. As in the case of condensed matter systems, sometimes there can be no gap at all. For example when $\epsilon(t) = \mu(t)$ but no longer real, one can verify that $E(t) = 1/\epsilon(t) \times \exp[\pm ikc \int_0^t 1/\epsilon(t') dt']$ is a solution to Maxwell's equations. So the dispersion curves are just straight lines $\omega = ck/T \times \int_0^T 1/\epsilon(t') dt'$. If $\int_0^T 1/\epsilon(t') dt'$ is real than they will stay in the real ω -real k plane.

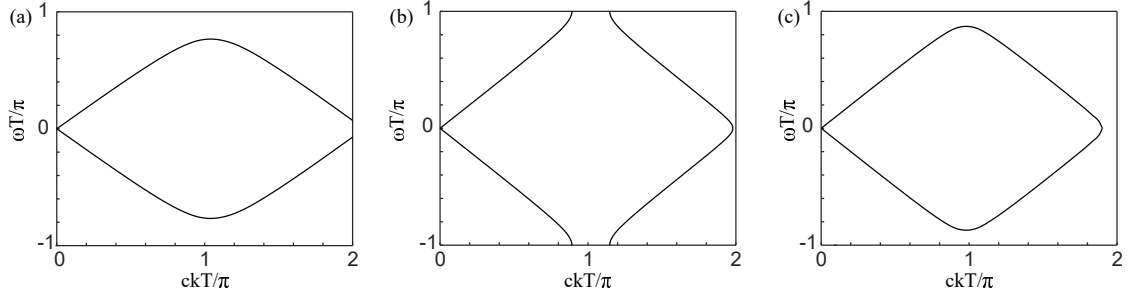


Figure 3.2: Various types of dispersion curves produced by periodic modulation of $\epsilon(t)$ and $\mu(t)$. (a) $\epsilon(t) = \mu^*(t) = 1 + 0.5i \cos(2\pi t/T)$. (b) $\epsilon(t) = 1/[1 + 0.5 \cos(2\pi t/T)]$, $\mu(t) = 1$. (c) $\epsilon(t) = 1/[1 + 0.5i \cos(2\pi t/T)]$, $\mu(t) = 1$.

The low-energy Hamiltonians of these systems near various band crossing points can be derived in a similar way as those of condensed matter models using perturbation theory.

One byproduct of all these analysis and examples emerges as soon as one realizes that under Floquet periodicity condition the temporal and spatial dimensions are treated equally. Since electromagnetism also has a similar dependence on time and space, the above results can be readily “translated” to conventional photonic crystals, when ϵ and μ vary periodically in space. In this case, if both $\epsilon, \mu \in \mathbb{R}$ then bandgaps are necessarily in quasienergy, which is the most familiar case. If $\epsilon(\mathbf{r}) = \mu^*(\mathbf{r})$ then bandgaps are necessarily in wavevector. Since μ is often difficult to manipulate, it’s more practical to add an imaginary modulation to $\epsilon(\mathbf{r})$ only, which can lead to bandgaps in both directions. For example, setting $\epsilon(x) = 1 + 0.5i \sin(2\pi x/L)$ in a one dimensional photonic crystal with period L will produce a band structure similar to Fig. 3.2(c), but with roles of frequency and wavevector exchanged. The parity-time symmetry $\epsilon(x) = \epsilon^*(-x)$ ensures most part of dispersion curves stays in the real ω -real k plane. This kind of modulation is utilized in a unidirectional reflectionless metamaterial [21]. The space-time duality also reminds us that exceptional points are actually ubiquitous: in a conventional

photonic crystal, whenever there is bandgap (in frequency), if one treats this as an eigenvalue problem for wavevector, then the band edges ω_{\pm} are exceptional points.

However, it should be noted that a gap in frequency or wavevector will have different consequences to the system. A wave in a frequency gap cannot propagate and will be reflected back, but a wave in a wavevector gap will actually grow exponentially. Similarly, an “interface” in space or time will lead to different behaviors of the system. That is because a system with an interface in space (maybe also under periodic driving) is subject to boundary conditions, while a system with an “interface” in time (for example, if one periodic driving changes into a different one) is subject to initial conditions. Therefore, for a FTI strip finite in y but infinite in x direction, given a k_x there will be some discrete frequencies (energies) in the gaps that support edge modes, but for two time crystals with different gap Zak phases connected back to back in time, all wavevectors in the common bandgap will lead to similar effects, namely the amplitude of the wave will first decrease and then grow again after the temporal interface [63], a phenomenon that can also be explained by parametric resonance [51].

3.5 Time-modulated SSH model

To finish the section, we offer a slightly more complicated model: an SSH model with time-modulated hopping amplitudes. This model is depicted in Fig. 3.3(a). The SSH model has two sublattices, A and B , in a unit cell. In a conventional SSH model, the intracell hopping amplitude v and intercell hopping amplitude w are both time-independent. If $|v| < |w|$ then the system is topologically trivial, and if $|v| < |w|$ then the system is topologically nontrivial (if $|v| = |w|$ then the system

is gapless). Now, we leave w unchanged but add (potentially non-Hermitian) time modulation to the intracell hopping amplitude: $v_{AB/BA}(t) = v_0 + a_{AB/BA}(t)$. Non-Hermitian SSH model has been discussed in, for example, Ref. [48, 54, 79, 95, 96], and the implementation of non-Hermitian hopping amplitudes has been proposed or realized in ultracold atom systems based on quantum decoherence theory [60, 75] and photonic systems by utilizing auxiliary rings with gain and loss, each added to half of a ring [61, 104].

Now back to our model. The momentum-space Hamiltonian is (assuming w real)

$$H(k, t) = \begin{pmatrix} 0 & v_{AB}(t) + we^{-ik} \\ v_{BA}(t) + we^{ik} & 0 \end{pmatrix}. \quad (3.9)$$

We choose $v_0 = -0.8w$, so that when the time modulation term $a(t)$ is turned off, the periodic spectrum of the system has a frequency gap around zero frequency at $k = 0$, see Fig. 3.3(b). Next we add a time modulation to the system. Specifically, we use $a_{AB}(t) = d \sin \Omega t$, $a_{BA}(t) = d \cos \Omega t$, which is similar to the A_3 mentioned above. When $d \approx 1.61$, the bandgap closes and the system becomes gapless, see Fig. 3.3(c). For larger d , the spectrum exhibits a gap in k at zero frequency, see Fig. 3.3(d). This example is similar to what happens at $\mathbf{G}_1 = (0, 0)$ point in Sec. 3.3, i.e., it can be explained by a second order perturbation theory.

We can also create a scenario that can be explained by a first order perturbation theory, i.e., similar to what happens at \mathbf{G}_2 point in Sec. 3.3. In this case we start with $v_0 = -0.2w$ and choose $\Omega = 2\pi/T = 2.4w$. Thus, after band folding, the two bands will touch at $k = \pi$ (see Fig. 3.4(a)), and by adding the same non-Hermitian time modulation $a_{AB}(t) = d \sin \Omega t$, $a_{BA}(t) = d \cos \Omega t$ we can create a gap in k , see Fig. 3.4(c). If we choose a k in this bandgap, the field in the system will grow exponentially, see Fig. 3.4(d). In this plot, we also introduced an “interface in

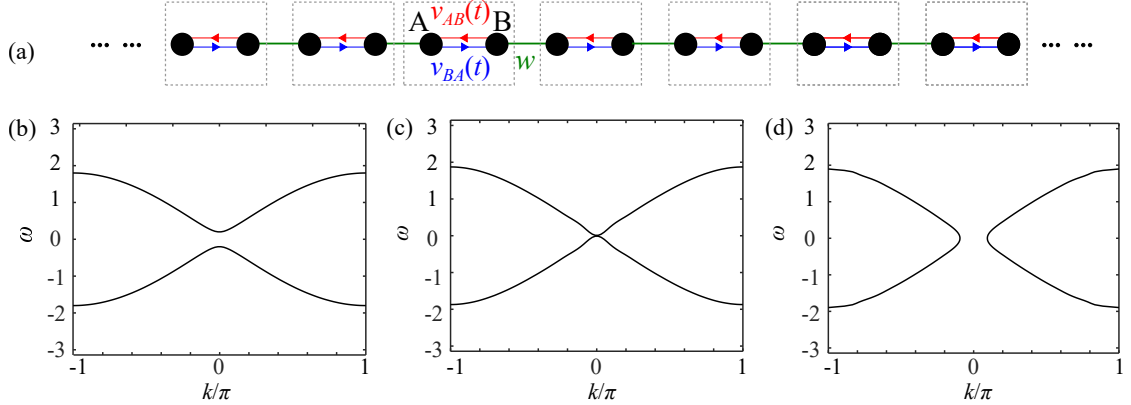


Figure 3.3: Dispersion curves of a time-modulated SSH model. (a) Illustration of a time-modulated SSH model. (b) The spectrum without time-modulation, corresponding to a conventional SSH model where intracell hopping amplitude $v_0 = -0.8w$. The bands are plotted within the first Brillouin zone of the quasi-wavevectors: $-\pi < k < \pi$. (c) A time-modulation on v can make the system gapless. Here $d = 1.61$. (d) An even stronger time-modulation makes the gap reopen, but in k . Here $d = 2$. Only modes with both real ω and real k are plotted. See text for explicit expressions of modulation $v_{AB/BA}(t)$ used. Parameters: $T = 1, w = 1$.

time” at $t = 50$, when the time modulation skips a phase π , see Fig. 3.4(b). The result is that the field immediately starts to decrease exponentially, thus creating a “edge state in time” [63]. Of course, eventually the field will start to grow exponentially again.

This phenomenon can be understood by calculating the growing and decaying eigenstates using perturbation theory. At $k = 0$, the perturbed states take the following form

$$\begin{pmatrix} e^{i\Omega t/2} \pm e^{-i\Omega t/2+i\theta} \\ (e^{i\Omega t/2} \mp e^{-i\Omega t/2+i\theta})e^{i\phi} \end{pmatrix} e^{\pm\gamma t}, \quad (3.10)$$

where $\phi = \arg(v_0 + we^{-ik})$, and θ is the phase difference of the two components of the eigenvectors of Eq. (3.6). In our case $\phi = 0$ and $\theta = \pi/4$. Plugging $t = 0$ the growing state takes the form $(1 + e^{i\pi/4}, 1 - e^{i\pi/4})^T$, and the decaying state takes the form $(1 - e^{i\pi/4}, 1 + e^{i\pi/4})^T$; while at $t = \pi$ the growing state takes the form $(i - ie^{i\pi/4}, i + ie^{i\pi/4})^T$, and the decaying state takes the form $(i + ie^{i\pi/4}, i - ie^{i\pi/4})^T$.

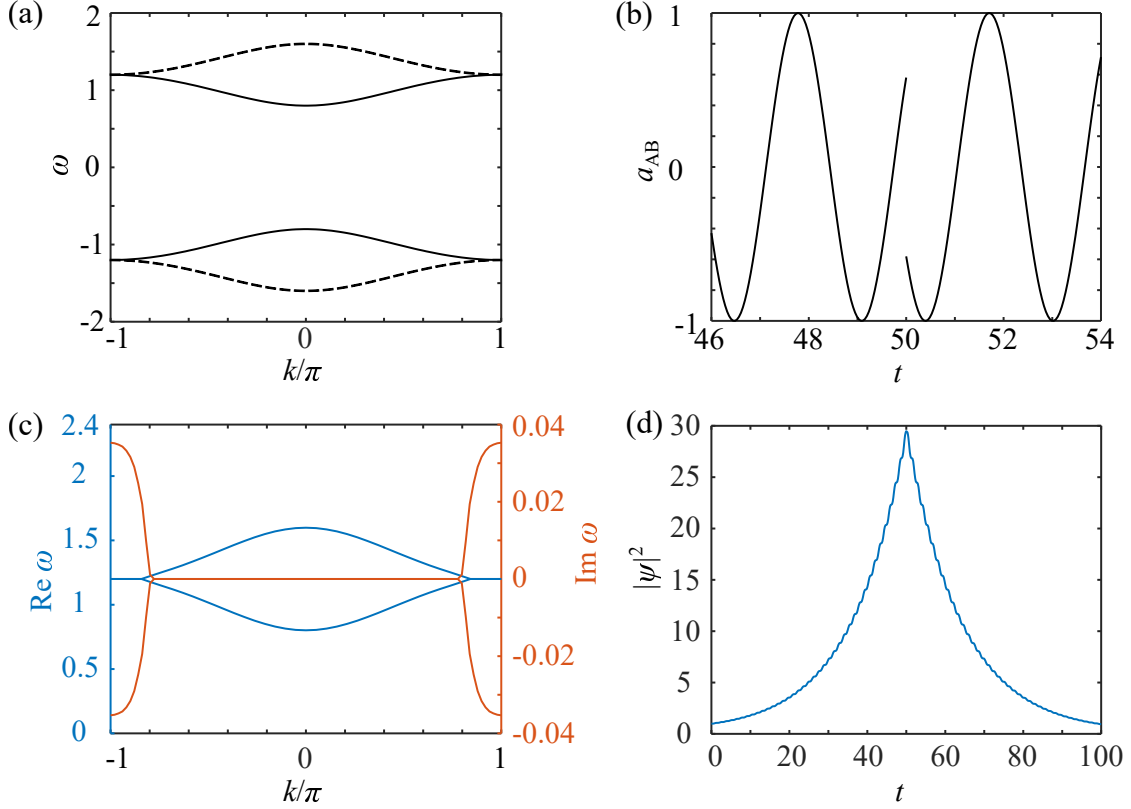


Figure 3.4: Another example of opening k -gaps in a time-modulated SSH model and using it to obtain an “edge state in time”. (a) Unperturbed band diagram ($d = 0$), including original SSH bands (solid) and additional bands due to artificial band folding (dashed). (b) Temporal modulation $a_{AB}(t)$. An interface is visible at $t = 50$. Here $d = 0.1$. (c) The real part and the imaginary part of the spectrum. The bands are plotted within the first Brillouin zone of the quasi-wavevectors: $-\pi < k < \pi$, as well as the first Floquet zone of the quasi-frequencies: $0 < \Re[\omega] < \Omega$. There are two exceptional points at $k \approx \pm 0.8\pi$. (d) A time domain simulation using $k = \pi$, inside the bandgap. At $t = 50$, the time modulation $a_{AB/BA}(t)$ skips a phase π . Thus, for $t > 50$, $a_{AB}(t) = -d \sin \Omega t$, $a_{BA}(t) = -d \cos \Omega t$. Parameters: $\Omega = 2.4$, $w = 1$, $v_0 = -0.2w$.

We can see that after the time modulation skips a phase π , the old growing state becomes the new decaying state, thus creating a “edge state in time”.

It is also possible to create a space-time corner mode, where the mode is localized both in space and time, by coupling two non-trivial SSH models, as shown in Fig. 3.5(a). The onsite potential of one of the chains is shifted away from zero by Ω . The non-Hermitian time modulation only connects A sites of both chains,

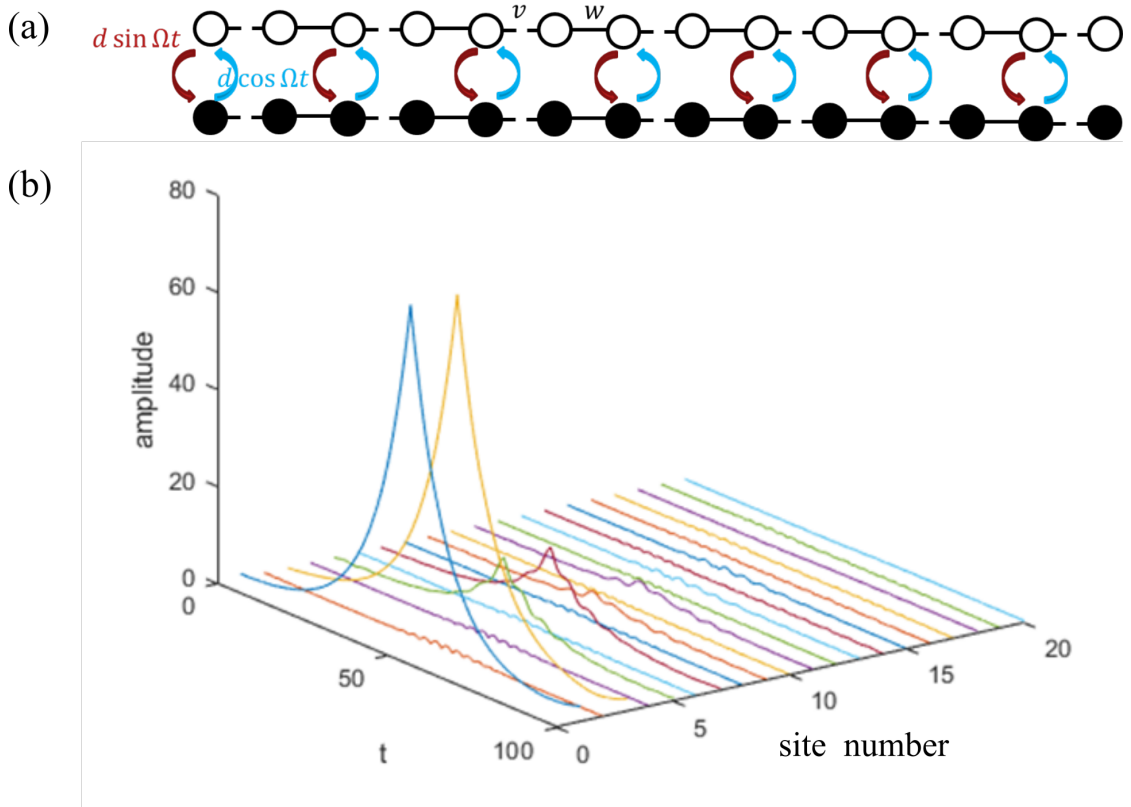


Figure 3.5: A space-time corner mode. (a) Ingredients: two finite non-trivial SSH chains, coupled by non-Hermitian hopping on A sites only. Their onsite potentials differ by Ω . (b) A time domain simulation. At $t = 50$, an interface in time similar to that in Fig. 3.4(d) is introduced. Parameters: $\Omega = 3, w = 1, v_0 = 0.2w, d = 0.1$. Total number of sites: 20 (5 unit cells).

therefore the two edge states at the left end will hybrid and their eigenfrequencies will become $\omega = \pm id$, while the two edge states at the right corner are unaffected and remain at $\omega = 0$ frequency. The bulk modes will also hybrid and acquire imaginary parts in their frequencies, but only half of that of the edge states at the left end $\omega = |v + we^{-ik}| \pm \frac{d}{2}i$. Therefore, after introducing an interface in time, we are able to see a mode that is localized both in space and time, shown in Fig. 3.5(b).

3.6 Conclusions

In conclusion, we investigate why FCs and PTCs have different types of bandgaps, and give criteria of bandgaps opening in quasienergy or wavevector, in both electromagnetism and condensed matter models, showing that FCs and PTCs are closely related. We also discuss the potential topology emerging from these models. We demonstrate that one can translate between a FC/PTC and a conventional photonic crystal, based on the similarities of periodic spatial and temporal modulation. At the same time, there are still notable differences between gaps in frequency or momentum, and an interface in space or time. We also point out the ubiquity of exceptional points in conventional band structures if the wavevector is treated as the eigenvalue, providing a new point of view to apply the knowledge of exceptional points.

BIBLIOGRAPHY

- [1] Giorgio Adamo, Jun-Yu Ou, JK So, SD Jenkins, F De Angelis, Kevin F MacDonald, E Di Fabrizio, J Ruostekoski, and Nikolay I Zheludev. Electron-beam-driven collective-mode metamaterial light source. *Phys. Rev. Lett.*, 109(21):217401, 2012.
- [2] X. Artru, G. B. Yodh, and G. Mennessier. Practical theory of the multilayered transition radiation detector. *Phys. Rev. D*, 12:1289–1306, Sep 1975.
- [3] J.K. Asbóth, L. Oroszlány, and A.P. Pályi. *A Short Course on Topological Insulators: Band Structure and Edge States in One and Two Dimensions*. Lecture Notes in Physics. Springer International Publishing, 2016.
- [4] Howard C. Baker. Non-hermitian quantum theory of multiphoton ionization. *Phys. Rev. A*, 30(2):773, 1984.
- [5] G. Bastard. *Wave mechanics applied to semiconductor heterostructures*. Monographies de physique. Les Éditions de Physique, 1988.
- [6] G. Bekefi, J. S. Wurtele, and I. H. Deutsch. Free-electron-laser radiation induced by a periodic dielectric medium. *Phys. Rev. A*, 34:1228, 1986.
- [7] Wladimir A Benalcazar, B Andrei Bernevig, and Taylor L Hughes. Quantized electric multipole insulators. *Science*, 357(6346):61–66, 2017.
- [8] Carl M Bender. Making sense of non-hermitian hamiltonians. *Rep. Prog. Phys.*, 70(6):947, 2007.
- [9] Carl M. Bender, Mariagiovanna Gianfreda, Şahin K. Özdemir, Bo Peng, and Lan Yang. Twofold transition in \mathcal{PT} -symmetric coupled oscillators. *Phys. Rev. A*, 88:062111, Dec 2013.
- [10] Michael V Berry. Physics of nonhermitian degeneracies. *Czechoslov. J. Phys.*, 54(10):1039–1047, 2004.
- [11] Fabio Biancalana, Andreas Amann, Alexander V Uskov, and Eoin P O’ reilly. Dynamics of light propagation in spatiotemporal dielectric structures. *Phys. Rev. E*, 75(4):046607, 2007.

- [12] CH Chen and J Silcox. Detection of optical surface guided modes in thin graphite films by high-energy electron scattering. *Phys. Rev. Lett.*, 35(6):389, 1975.
- [13] Hua-Zhou Chen, Tuo Liu, Hong-Yi Luan, Rong-Juan Liu, Xing-Yuan Wang, Xue-Feng Zhu, Yuan-Bo Li, Zhong-Ming Gu, Shan-Jun Liang, He Gao, et al. Revealing the missing dimension at an exceptional point. *Nature Physics*, 16(5):571–578, 2020.
- [14] Wen-Jie Chen, Shao-Ji Jiang, Xiao-Dong Chen, Baocheng Zhu, Lei Zhou, Jian-Wen Dong, and Che Ting Chan. Experimental realization of photonic topological insulator in a uniaxial metacrystal waveguide. *Nat. Commun.*, 5:5782, 2014.
- [15] P. A. Cherenkov. *Dokl. Akad. Nauk SSSR*, 2:457, 1934.
- [16] Michael L. Cherry, Gernot Hartmann, Dietrich Müller, and Thomas A. Prince. Transition radiation from relativistic electrons in periodic radiators. *Phys. Rev. D*, 10:3594–3607, Dec 1974.
- [17] FJ García De Abajo. Optical excitations in electron microscopy. *Rev. Mod. Phys.*, 82(1):209, 2010.
- [18] Ramy El-Ganainy, Konstantinos G Makris, Mercedeh Khajavikhan, Ziad H Musslimani, Stefan Rotter, and Demetrios N Christodoulides. Non-hermitian physics and pt symmetry. *Nat. Phys.*, 14(1):11–19, 2018.
- [19] Motohiko Ezawa. Photoinduced topological phase transition and a single dirac-cone state in silicene. *Phys. Rev. Lett.*, 110(2):026603, 2013.
- [20] Liang Feng, Ramy El-Ganainy, and Li Ge. Non-hermitian photonics based on parity-time symmetry. *Nat. Phot.*, 11:752, 2017.
- [21] Liang Feng, Ye-Long Xu, William S Fegadolli, Ming-Hui Lu, José EB Oliveira, Vilson R Almeida, Yan-Feng Chen, and Axel Scherer. Experimental demonstration of a unidirectional reflectionless parity-time metamaterial at optical frequencies. *Nat. Mat.*, 12(2):108, 2013.
- [22] Romain Fleury, Alexander B. Khanikaev, and Andrea Alu. Floquet topological insulators for sound. *Nature Comm.*, 7:7:11744, June 2016.

- [23] George W Ford and Willes H Weber. Electromagnetic interactions of molecules with metal surfaces. *Phys. Rep.*, 113(4):195–287, 1984.
- [24] I. M. Frank and V. L. Ginzburg. *J. Phys. (Moscow)*, 9:353, 1945.
- [25] J M Frank. *Acta Phys. Pol.*, A 38:655, 1970.
- [26] G M Garibian. In *Proc. Conf. High Energy Physics Instrumentation*, volume 2, page 509, Dubna, 1970.
- [27] V.L. Ginzburg and V.N. Tsytovich. *Transition radiation and transition scattering*. Adam Hilger, Bristol and New York, 1990.
- [28] D. M. Goebel, J. M. Butler, R. W. Schumacher, J. Santoru, and R. L. Eisenhart. High-power microwave source based on an unmagnetized backward-wave oscillator. *IEEE Trans. Plasma Sci.*, 22:547, 1994.
- [29] Gene H Golub and Charles F Van Loan. *Matrix computations*. Johns Hopkins University Press, 4th edition, 2013.
- [30] Mohammad Hafezi, Eugene A Demler, Mikhail D Lukin, and Jacob M Taylor. Robust optical delay lines with topological protection. *Nat. Phys.*, 7(11):907, 2011.
- [31] Mohammad Hafezi, S Mittal, J Fan, A Migdall, and JM Taylor. Imaging topological edge states in silicon photonics. *Nat. Photonics*, 7(12):1001, 2013.
- [32] U. Happek, A. J. Sievers, and E. B. Blum. Observation of coherent transition radiation. *Phys. Rev. Lett.*, 67:2962–2965, Nov 1991.
- [33] Absar U. Hassan, Bo Zhen, Marin Soljačić, Mercedeh Khajavikhan, and Demetrios N. Christodoulides. Dynamically encircling exceptional points: Exact evolution and polarization state conversion. *Phys. Rev. Lett.*, 118:093002, Mar 2017.
- [34] Li He, Zachariah Addison, Jicheng Jin, Eugene J Mele, Steven G Johnson, and Bo Zhen. Floquet chern insulators of light. *Nat. Commun.*, 10:4194, 2019.
- [35] WD Heiss. Exceptional points of non-hermitian operators. *J. Phys. Math. Gen.*, 37(6):2455, 2004.

- [36] D Holberg and K Kunz. Parametric properties of fields in a slab of time-varying permittivity. *IEEE Trans. Antennas Propag.*, 14(2):183–194, 1966.
- [37] L. Jin and Z. Song. Bulk-boundary correspondence in a non-hermitian system in one dimension with chiral inversion symmetry. *Phys. Rev. B*, 99:081103, Feb 2019.
- [38] John D. Joannopoulos, Steven G. Johnson, Joshua N. Winn, and Robert D. Meade. *Photonic Crystals: Molding the Flow of Light*. Princeton University Press, Princeton and Oxford, 2 edition, 2008.
- [39] John D Joannopoulos, Pierre R Villeneuve, and Shanhui Fan. Photonic crystals. *Solid State Communications*, 102(2-3):165–173, 1997.
- [40] Sajeev John. Strong localization of photons in certain disordered dielectric superlattices. *Phys. Rev. Lett.*, 58:2486, 1987.
- [41] Ido Kaminer, SE Kooi, R Shiloh, B Zhen, Y Shen, JJ López, R Remez, SA Skirlo, Y Yang, JD Joannopoulos, et al. Spectrally and spatially resolved smith-purcell radiation in plasmonic crystals with short-range disorder. *Phys. Rev. X*, 7(1):011003, 2017.
- [42] Kohei Kawabata, Ken Shiozaki, and Masahito Ueda. Anomalous helical edge states in a non-hermitian chern insulator. *Phys. Rev. B*, 98:165148, Oct 2018.
- [43] S Yu Kazakov, SV Kuzikov, Y Jiang, and JL Hirshfield. High-gradient two-beam accelerator structure. *Phys. Rev. ST Accel. Beams*, 13(7):071303, 2010.
- [44] Alexander B Khanikaev, S Hossein Mousavi, Wang-Kong Tse, Mehdi Kar-garian, Allan H MacDonald, and Gennady Shvets. Photonic topological insulators. *Nat. Mat.*, 12(3):233, 2013.
- [45] Takuya Kitagawa, Erez Berg, Mark Rudner, and Eugene Demler. Topological characterization of periodically driven quantum systems. *Phys. Rev. B*, 82(23):235114, 2010.
- [46] Takuya Kitagawa, Takashi Oka, Arne Brataas, Liang Fu, and Eugene Demler. Transport properties of nonequilibrium systems under the application of light: Photoinduced quantum hall insulators without landau levels. *Phys. Rev. B*, 84(23):235108, 2011.
- [47] Christian Kremers, Dmitry N. Chigrin, and Johann Kroha. Theory of

- cherenkov radiation in periodic dielectric media: Emission spectrum. *Phys. Rev. A*, 79:013829, Jan 2009.
- [48] Flore K. Kunst, Elisabet Edvardsson, Jan Carl Budich, and Emil J. Bergholtz. Biorthogonal bulk-boundary correspondence in non-hermitian systems. *Phys. Rev. Lett.*, 121:026808, Jul 2018.
- [49] Martin Kuttge, Ernst Jan R Vesseur, A F Koenderink, H J Lezec, H A Atwater, F J García de Abajo, and Albert Polman. Local density of states, spectrum, and far-field interference of surface plasmon polaritons probed by cathodoluminescence. *Phys. Rev. B*, 79(11):113405, 2009.
- [50] Kueifu Lai, Tzuhsuan Ma, Xiao Bo, Steven Anlage, and Gennady Shvets. Experimental realization of a reflections-free compact delay line based on a photonic topological insulator. *Sci. Rep.*, 6:28453, 2016.
- [51] L. D. Landau and E. M. Lifshitz. *Mechanics*. Butterworth-Heinemann, 3rd edition, 1976.
- [52] Lev Davidovich Landau, JS Bell, MJ Kearsley, LP Pitaevskii, EM Lifshitz, and JB Sykes. *Electrodynamics of continuous media*, volume 8. elsevier, 2013.
- [53] Lev Davidovich Landau and Evgenii Mikhailovich Lifshitz. *Quantum mechanics: non-relativistic theory*, volume 3. Elsevier, 2013.
- [54] Tony E Lee. Anomalous edge state in a non-hermitian lattice. *Phys. Rev. Lett.*, 116(13):133903, 2016.
- [55] Linhu Li, Muhammad Umer, and Jiangbin Gong. Direct prediction of corner state configurations from edge winding numbers in two- and three-dimensional chiral-symmetric lattice systems. *Phys. Rev. B*, 98:205422, Nov 2018.
- [56] Simon Lieu. Topological phases in the non-hermitian su-schrieffer-heeger model. *Phys. Rev. B*, 97(4):045106, 2018.
- [57] Xiao Lin, Sajan Easo, Yichen Shen, Hongsheng Chen, Baile Zhang, John D Joannopoulos, Marin Soljačić, and Ido Kaminer. Controlling cherenkov angles with resonance transition radiation. *Nat. Phys.*, 14(8):816, 2018.

- [58] Netanel H Lindner, Gil Refael, and Victor Galitski. Floquet topological insulator in semiconductor quantum wells. *Nat. Phys.*, 7(6):490, 2011.
- [59] Tao Liu, Yu-Ran Zhang, Qing Ai, Zongping Gong, Kohei Kawabata, Masahito Ueda, and Franco Nori. Second-order topological phases in non-hermitian systems. *Phys. Rev. Lett.*, 122(7):076801, 2019.
- [60] Tao Liu, Yu-Ran Zhang, Qing Ai, Zongping Gong, Kohei Kawabata, Masahito Ueda, and Franco Nori. Second-order topological phases in non-hermitian systems. *Phys. Rev. Lett.*, 122:076801, Feb 2019.
- [61] Stefano Longhi, Davide Gatti, and Giuseppe Della Valle. Robust light transport in non-hermitian photonic lattices. *Scientific reports*, 5(1):1–12, 2015.
- [62] Kenneth Lopata and Niranjan Govind. Near and above ionization electronic excitation with non-hermitian real-time time-dependent density functional theory. *J. Chem. Th. and Comp.*, 9:4939, 2013.
- [63] Eran Lustig, Yonatan Sharabi, and Mordechai Segev. Topological aspects of photonic time crystals. *Optica*, 5(11):1390–1395, 2018.
- [64] Tzuhsuan Ma, Alexander B. Khanikaev, S. Hossein Mousavi, and Gennady Shvets. Guiding electromagnetic waves around sharp corners: Topologically protected photonic transport in metawaveguides. *Phys. Rev. Lett.*, 114:127401, Mar 2015.
- [65] Tzuhsuan Ma and Gennady Shvets. All-si valley-hall photonic topological insulator. *New J. Phys.*, 18(2):025012, 2016.
- [66] A. McDonald, T. Pereg-Barnea, and A. A. Clerk. Phase-dependent chiral transport and effective non-hermitian dynamics in a bosonic kitaev-majorana chain. *Phys. Rev. X*, 8:041031, Nov 2018.
- [67] Nimrod Moiseyev. *Non-Hermitian quantum mechanics*. Cambridge University Press, 2011.
- [68] Ali Mostafazadeh. Pseudo-hermiticity versus pt symmetry: the necessary condition for the reality of the spectrum of a non-hermitian hamiltonian. *J. Math. Phys.*, 43(1):205–214, 2002.
- [69] Xiang Ni, Matthew Weiner, Andrea Alù, and Alexander B Khanikaev. Ob-

servation of higher-order topological acoustic states protected by generalized chiral symmetry. *Nat. Mat.*, 18(2):113, 2019.

- [70] Konstantin S Novoselov, VI Fal, L Colombo, PR Gellert, MG Schwab, K Kim, et al. A roadmap for graphene. *nature*, 490(7419):192–200, 2012.
- [71] B. Pardo and J-M. André. Transition radiation from periodic stratified structures. *Phys. Rev. A*, 40:1918–1925, Aug 1989.
- [72] M. A. Piestrup and P. F. Finman. *IEEE J. Quantum Electron.*, QE-19:357, 1983.
- [73] Filipa R. Prudêncio and Mário G. Silveirinha. Asymmetric cherenkov emission in a topological plasmonic waveguide. *Phys. Rev. B*, 98:115136, Sep 2018.
- [74] Mikael C Rechtsman, Julia M Zeuner, Yonatan Plotnik, Yaakov Lumer, Daniel Podolsky, Felix Dreisow, Stefan Nolte, Mordechai Segev, and Alexander Szameit. Photonic floquet topological insulators. *Nature*, 496(7444):196, 2013.
- [75] Florentin Reiter and Anders S. Sørensen. Effective operator formalism for open quantum systems. *Phys. Rev. A*, 85:032111, Mar 2012.
- [76] Kazuaki Sakoda. *Optical Properties of Photonic Crystals*. Springer-Verlag, Berlin Heidelberg, 2005.
- [77] Henning Schomerus. Nonreciprocal response theory of non-hermitian mechanical metamaterials: Response phase transition from the skin effect of zero modes. *Phys. Rev. Research*, 2:013058, Jan 2020.
- [78] M. A. Shapiro, S. Trendafilov, Y. Urzhumov, A. Al‘u, R. J. Temkin, and G. Shvets. Active negative-index metamaterial powered by an electron beam. *Phys. Rev. B*, 86:085132, 2012.
- [79] Huitao Shen, Bo Zhen, and Liang Fu. Topological band theory for non-hermitian hamiltonians. *Phys. Rev. Lett.*, 120:146402, Apr 2018.
- [80] Aleksandr B Shvartsburg. Optics of nonstationary media. *Phys. Usp.*, 48(8):797, 2005.

- [81] Evgenya I Smirnova, Amit S Kesar, Ivan Mastovsky, Michael A Shapiro, and Richard J Temkin. Demonstration of a 17-ghz, high-gradient accelerator with a photonic-band-gap structure. *Phys. Rev. Lett.*, 95(7):074801, 2005.
- [82] Hadas Soifer, Alexandre Gauthier, Alexander F Kemper, Costel R Rotundu, Shuolong Yang, Hongyu Xiong, Donghui Lu, Makoto Hashimoto, Patrick S Kirchmann, Jonathan A Sobota, et al. Band resolved imaging of photocurrent in a topological insulator. *Phys. Rev. Lett.*, 2017.
- [83] W_P Su, JR Schrieffer, and Ao J Heeger. Solitons in polyacetylene. *Physical review letters*, 42(25):1698, 1979.
- [84] M L Ter-Mikaelian. *High Energy Electromagnetic Processes in Condensed Media*. Wiley, New York, 1972.
- [85] S. E. Tsimring. *Electron beams and microwave vacuum electronics*. John Wiley and Sons, Inc., Hoboken, New Jersey, 2007.
- [86] M Wada, S Murakami, F Freimuth, and G Bihlmayer. Localized edge states in two-dimensional topological insulators: Ultrathin bi films. *Phys. Rev. B*, 83(12):121310, 2011.
- [87] L Wartski, S Roland, J Lasalle, M Bolore, and G Filippi. Interference phenomenon in optical transition radiation and its application to particle beam diagnostics and multiple-scattering measurements. *J. Appl. Phys.*, 46(8):3644–3653, 1975.
- [88] Carl T. West, Tsampikos Kottos, and Tomaž Prosen. \mathcal{PT} -symmetric wave chaos. *Phys. Rev. Lett.*, 104:054102, Feb 2010.
- [89] D. H. Whittum and S. G. Tantawi. Switched matrix accelerator. *Rev. Sci. Instrum.*, 72:73, 2001.
- [90] David H Whittum. Introduction to electrodynamics for microwave linear accelerators. In *Frontiers of Accelerator Technology*, pages 1–135. World Scientific, 1999.
- [91] Gregory Wilson, John Robert Dennison, Amberly Evans Jensen, and Justin Dekany. Electron energy-dependent charging effects of multilayered dielectric materials. *IEEE Trans. Plasma Sci.*, 41(12):3536–3544, 2013.

- [92] Z. Wu and A. Grbic. Serrodyne frequency translation using time-modulated metasurfaces. *IEEE Trans. Antennas Propag.*, 68(3):1599–1606, 2020.
- [93] Eli Yablonovitch. Inhibited spontaneous emission in solid-state physics and electronics. *Phys. Rev. Lett.*, 58:2059, 1987.
- [94] Naoki Yamamoto, F Javier García de Abajo, and Viktor Myroshnychenko. Interference of surface plasmons and smith-purcell emission probed by angle-resolved cathodoluminescence spectroscopy. *Phys. Rev. B*, 91(12):125144, 2015.
- [95] Shunyu Yao, Fei Song, and Zhong Wang. Non-hermitian chern bands. *Phys. Rev. Lett.*, 121:136802, Sep 2018.
- [96] Shunyu Yao and Zhong Wang. Edge states and topological invariants of non-hermitian systems. *Phys. Rev. Lett.*, 121(8):086803, 2018.
- [97] Shunyu Yao, Zhongbo Yan, and Zhong Wang. Topological invariants of floquet systems: General formulation, special properties, and floquet topological defects. *Phys. Rev. B*, 96:195303, Nov 2017.
- [98] Chuanhao Yin, Hui Jiang, Linhu Li, Rong Lü, and Shu Chen. Geometrical meaning of winding number and its characterization of topological phases in one-dimensional chiral non-hermitian systems. *Phys. Rev. A*, 97(5):052115, 2018.
- [99] Yang Yu, Minwoo Jung, and Gennady Shvets. Zero-energy corner states in a non-hermitian quadrupole insulator. *Phys. Rev. B*, 103:L041102, Jan 2021.
- [100] Yang Yu, Minwoo Jung, and Gennady Shvets. Zero-energy corner states in a non-hermitian quadrupole insulator. *Physical Review B*, 103(4), Jan 2021.
- [101] Yang Yu, Kueifu Lai, Jiahang Shao, John Power, Manoel Conde, Wanming Liu, Scott Doran, Chunguang Jing, Eric Wisniewski, and Gennady Shvets. Transition radiation in photonic topological crystals: Quasiresonant excitation of robust edge states by a moving charge. *Phys. Rev. Lett.*, 123:057402, Jul 2019.
- [102] Aycan Yurtsever, Martin Couillard, and David A Muller. Formation of guided cherenkov radiation in silicon-based nanocomposites. *Phys. Rev. Lett.*, 100(21):217402, 2008.

- [103] J Zak. Berry' s phase for energy bands in solids. *Physical review letters*, 62(23):2747, 1989.
- [104] Xueyi Zhu, Huaiqiang Wang, Samit Kumar Gupta, Haijun Zhang, Biye Xie, Minghui Lu, and Yanfeng Chen. Photonic non-hermitian skin effect and non-bloch bulk-boundary correspondence. *Phys. Rev. Research*, 2:013280, Mar 2020.
- [105] Jorge R Zurita-Sánchez, JH Abundis-Patiño, and P Halevi. Pulse propagation through a slab with time-periodic dielectric function ϵ (t). *Opt. Express*, 20(5):5586–5600, 2012.
- [106] Jorge R Zurita-Sánchez, P Halevi, and Juan C Cervantes-Gonzalez. Reflection and transmission of a wave incident on a slab with a time-periodic dielectric function (t). *Phys. Rev. A*, 79(5):053821, 2009.